ETH
Eidgenössische Technische Hochschule Zürich
Swiss Federal Institute of Technology Zurich

IAC Institute for Atmospheric and Climate Science

Master Thesis

Marine boundary layer stable water isotope variability in the Southern Ocean

An investigation using the regional $COSMO_{iso}$ model

Department of Earth Sciences, ETH Zurich
Institute for Atmospheric and Climate Science

Dr. Franziska Aemisegger, Institute for Atmospheric and Climate Science, ETH Zurich
(main advisor)
Iris Thurnherr, Institute for Atmospheric and Climate Science, ETH Zurich
Fabienne Dahinden, Institute for Atmospheric and Climate Science, ETH Zurich

Submitted by

Lukas Jansing
14-915-888
Zurich, March 26, 2019

Abstract

The Southern Ocean overturning strength constitutes an essential control mechanism for future anthropogenic carbon uptake. The atmospheric water cycle, in turn, exerts an influence on upwelling intensity via buoyancy forcing induced by freshwater fluxes. Stable water isotopes ($H_2{}^{16}O$, $H_2{}^{18}O$, HDO) are a powerful tool to constrain processes of the atmospheric water cycle and can therefore help to gain a more comprehensive picture on the Southern Ocean region. In order to fully exploit this potential, simulations with the isotope-enabled, regional numerical model $COSMO_{iso}$ are combined with isotope and meteorological measurements of high temporal resolution, conducted during the Antarctic Circumnavigation Expedition (ACE) in austral summer 2016/2017. For the first time, the $COSMO_{iso}$ model performance with respect to meteorology and stable water isotopes is assessed in the Southern Hemisphere, along Leg 1 and Leg 2 of ACE. The validation confirms a reliable representation of meteorology and isotope processes over the open ocean, but reveals model shortcomings with respect to isotopic variability in proximity to the Antarctic continent. Non-fractionating snow-atmosphere interactions are identified as a main factor limiting the model performance. Consequently, the implementation of equilibrium fractionation during surface snow sublimation and deposition improves the skill of $COSMO_{iso}$ significantly (correlation increases from 0.1 to 0.7 for δ-variables). This points out the potential of further model development in order to reproduce the entire spectrum of processes affecting stable water isotopic variability in polar regions with $COSMO_{iso}$. Furthermore, a newly developed Lagrangian budget model for isotopes and humidity is presented. The model framework incorporates the processes of horizontal advection, ocean evaporation and marine boundary layer mixing. In a first, exploratory case study, the air parcel-based box model is used to study the isotopic signal along trajectories associated with a marine cold air outbreak. By comparing the box model simulations to $COSMO_{iso}$, entrainment of depleted, free-tropospheric air is identified as an important factor, besides ocean evaporation, influencing the observed isotopic variability during the event. Downward mixing of air masses from the lower troposphere efficiently replaces the original Antarctic moisture along the transport pathway. The box model framework is a promising starting point for future efforts to further constrain the marine boundary layer moisture budget.

Contents

Chapter 1

Introduction

1.1 Importance of the Southern Ocean

The Southern Ocean (SO) as the water mass surrounding Antarctica plays a key role in the Earth's climate system. It interconnects the three major ocean basins and serves as an exchange interface between the deep ocean and the atmosphere (Morrison et al., 2015). The surface freshwater budget of the SO exerts an influence on its density stratification (Stössel et al., 2015), which in turn affects future uptake of anthropogenic CO_2. Precipitation and evaporation, adding up to the surface freshwater budget, are tightly linked to mid-latitude and polar weather systems, for instance via cold and warm air advection associated with extratropical cyclones or cold air outbreaks (Papritz et al., 2015). It is, therefore, important to improve our understanding of the atmospheric water cycle and its synoptic drivers in this region in order to gain a more comprehensive picture of freshwater fluxes between the ocean and the atmosphere. Furthermore, the SO is an important moisture source region for Antarctic precipitation (Sodemann and Stohl, 2009). Measured ratios of stable water isotopes (SWIs) in ice cores are widely used proxies for paleoclimatic reconstructions. The SWI composition of the arriving precipitation is influenced by the conditions during ocean evaporation and subsequently modified along the transport pathway. An advanced knowledge of processes affecting the SWI signal thus facilitates the interpretation of ice core measurements.

The next Sections will introduce SWIs as useful tracers to investigate the variability of freshwater fluxes at the air-sea interface. First, a few definitions relating to SWIs

will be introduced in Section 1.2, and then, in Section 1.3, existing isotope-enabled numerical models and their use will be shortly reviewed.

1.2 Stable water isotopes

SWIs as naturally available tracers are not only used in paleoclimatology, but serve also as a powerful tool to investigate moist processes in all parts of the hydrological cycle, including its atmospheric branch (Dansgaard, 1964). An excellent review in terms of possible applications of SWIs in the atmospheric water cycle is given in Galewsky et al. (2016).

The stable isotopes of oxygen and hydrogen can be combined to nine possible molecules, so called isotopologues. The three most important combinations, commonly referred to as stable isotopes of water, are $H_2{}^{16}O$, $H_2{}^{18}O$ and $HD^{16}O$. Their relative abundance is given in Table 1 (Sharp, 2007; Galewsky et al., 2016):

$H_2{}^{16}O$	$H_2{}^{18}O$	$HD^{16}O$
99.73098%	0.199978%	0.031460%

Table 1. Relative abundance of the three most important SWIs.

Due to their small relative abundances, the heavy isotopologues are commonly referred to as ratios (R) of the concentrations of the heavy (e.g. here $[H_2{}^{18}O]$) to the light isotope ($[H_2{}^{16}O]$):

$$ {}^{18}R = \frac{[H_2{}^{18}O]}{[H_2{}^{16}O]} \tag{1} $$

In order to quantify isotopic enrichment or depletion relative to a standard reservoir and for measurement purposes, SWIs are additionally expressed in the δ-notation, meaning with respect to the isotope ratio of Vienna Standard Mean Ocean Water (RVSMOW) from the International Atomic Energy Agency (IAEA):

$$ \delta^{18}O = \left(\frac{{}^{18}R_{sample}}{{}^{18}R_{VSMOW}} - 1 \right) \cdot 1000‰ \tag{2} $$

This definition implies that ocean water has $\delta^{18}O$ and $\delta^{2}H$ values of approximately 0‰, and atmospheric vapour is generally depleted relative to the ocean water. Dur-

ing phase transitions, water molecules are partitioned into the different phases according to their isotopic composition. The heavy isotopologues preferentially enter the condensed phase during condensation or stay in it during evaporation. This effect, referred to as isotopic fractionation, is caused by two different physical properties of water molecules. First of all, SWIs vary with respect to their intermolecular binding energies and thus also their saturation vapour pressures. Fractionation due to this effect is called equilibrium fractionation. It leads to lower concentrations of heavy isotopes in the vapour and strongly depends on temperature. Furthermore, unequal diffusion velocities of the heavy isotopologues lead to additional fractionation whenever a system is not in thermodynamic equilibrium. This frequently occurs in the Earth's atmosphere, e.g. during ocean evaporation into a ventilated environment. Since equilibrium fractionation relates variations in δ^2H and δ^{18}O by a relatively constant factor of 8, the second-order isotope variable deuterium excess (d-excess) can be defined as a measure for non-equilibrium effects (Dansgaard, 1964):

$$\text{d-excess} = \delta\text{D} - 8 \cdot \delta^{18}\text{O} \tag{3}$$

SWIs can serve to trace phase transitions in the hydrological cycle. Figure 1 shows the numerous processes affecting the isotopic composition of water vapour in the atmosphere. During the cycling of water through the Earth's atmosphere, the SWI composition is directly affected by the fractionating processes of evaporation from ocean surfaces, cloud formation and rain evaporation during falling precipitation. The ocean provides a reservoir with a large abundance of heavy isotopes relative to the atmosphere. Therefore, freshly formed evaporate can lead to enrichment of the marine boundary layer (MBL) vapour (see red arrow in Fig. 1). During rain evaporation, on the other hand, the preferential transfer of light isotopes typically depletes the surrounding vapour while enriching the residual precipitation (see blue arrow in Fig. 1). However, it has to be emphasized that the influence of precipitation evaporation on the ambient vapour is strongly variable in time and depends on the drop size distribution and intensity of precipitation amongst others (Graf et al., 2019). Condensation in clouds depletes the remaining vapour as well. Ocean evaporation and re-evaporation of condensate falling through unsaturated air are strongly tied to non-equilibrium effects, while cloud droplet formation is

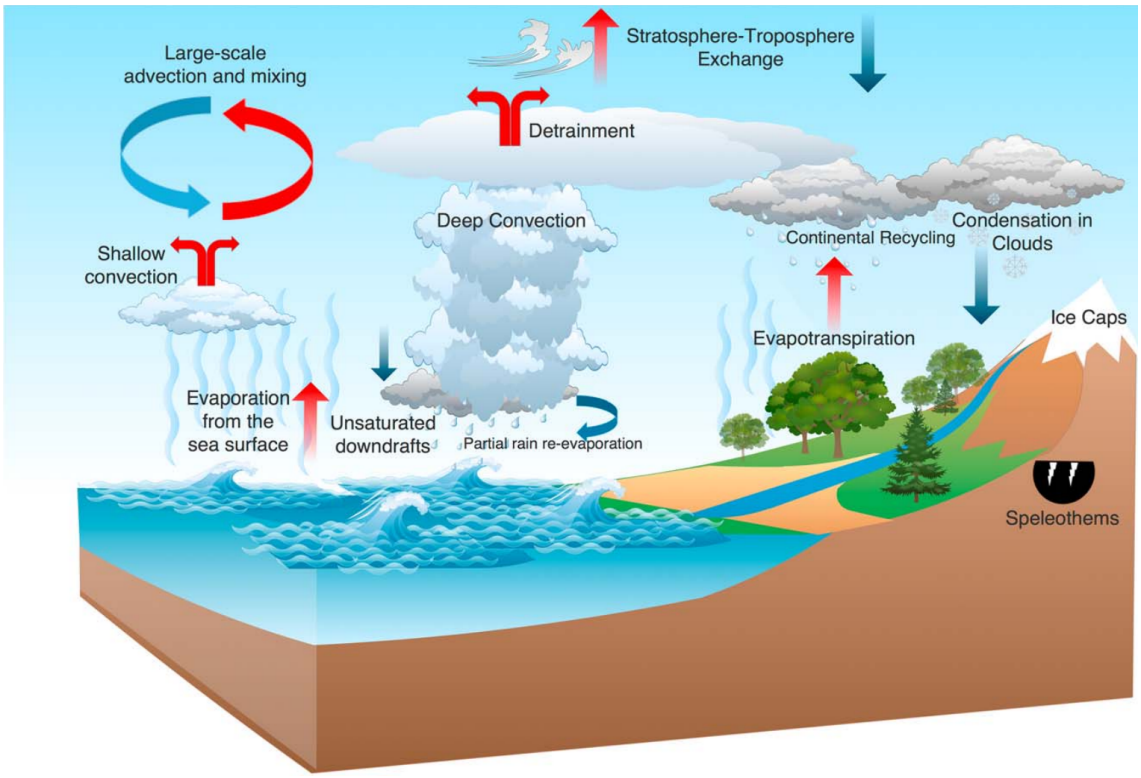

Fig. 1. Illustration from Galewsky et al. (2016) showing different processes in the atmosphere that affect the isotopic composition of water vapour. Red indicates enriching, blue depleting processes.

approximately an equilibrium process. Air masses with different origin are characterised by distinct isotopic signatures. Therefore, besides being related directly to processes that involve phase changes, SWIs can also give indirect constraints on the non-fractionating processes of entrainment of free tropospheric air into the MBL or transitions in isotope signals induced by changes in the large-scale horizontal advection of air (Fig. 1).

Isotopic fractionation during evaporation from a water surface can be described by the Craig-Gordon model (C-G model), first formulated by Craig and Gordon (1965). The C-G model is a multi-layer model for the evaporation flux from a water body into the atmosphere. It comprises both equilibrium fractionation and non-equilibrium effects. An extensive overview on the physical background and the applicability for different interfaces can be found in Horita et al. (2008). The C-G model predicts the isotopic evaporation flux from a water body by the following equation:

$$R_e = \frac{\frac{R_l}{\alpha} - h_S \cdot R_v}{\alpha_k \cdot (1 - h_S)} \tag{4}$$

According to the C-G model, the isotopic composition of vapour formed by evaporation thus depends on the isotopic composition of the surface ocean water (R_l), the isotopic composition of the MBL vapour (R_v), the relative humidity with respect to sea surface temperature (h_S), the equilibrium fractionation factor (α) and the non-equilibrium fractionation factor (α_k) that includes the effect of differing diffusivities of the heavy isotopologues. The main limitation of the C-G model concerns its zero-dimensional character: It neglects both height-dependent entrainment of free-tropospheric air into the MBL as well as horizontal advection. Despite this shortcoming, the C-G model has been established as a cornerstone in different studies investigating evaporation-dominated systems (e.g. Aemisegger et al., 2014; Aemisegger and Sjolte, 2018) and the MBL moisture budget (e.g. Benetti et al., 2015). Merlivat and Jouzel (1979) simplified (4) assuming a globally balanced water budget, referred to as the closure assumption. Under their assumption, the isotopic flux of evaporation is equal the MBL composition itself ($R_v = R_e$) and the C-G model simplifies to:

$$R_e = \frac{R_l}{\alpha \cdot \Big(\alpha_k + h_S \cdot (1 - \alpha_k)\Big)} \tag{5}$$

Recently, several new model frameworks have been presented including the effect of vertical mixing into the MBL (Benetti et al., 2018; Feng et al., 2018). It has yet to be assessed how they compare to the established C-G and closure model for different dynamical situations. This is one of the primary motivations for Section 3.3, where evaporation and MBL mixing will be studied in a Lagrangian framework for a strong evaporation event in the Ross Sea.

To describe isotopic fractionation along an idealized, precipitating trajectory, the Rayleigh distillation model is a useful tool (Dansgaard, 1964). It describes the temporal development of the isotopic composition of condensate formed in a cooling and precipitating air parcel as well as the composition of the more and more depleted residual vapour assuming it to be an equilibrium process. For a further

description and extension of the classical Rayleigh distillation model I refer to Gat (1996).

SWI measurements deliver information on the integrated history of moisture in an air parcel. Observations with a high temporal resolution are a useful approach to study SWI variability of synoptic-scale weather systems. These observations have been made possible with the advent of commercial laser spectrometer, which can easily be deployed in the field (e.g. Aemisegger et al., 2012; Wei et al., 2019). They can be used to characterize moisture source conditions over the ocean (e.g. Pfahl and Wernli, 2008) and the land surface (e.g. Aemisegger et al., 2014) or trace phase changes within weather systems (Aemisegger et al., 2015; Dütsch et al., 2018).

1.3 The role of isotope-enabled models

The SWI signal of in-situ measurements contains the integrated history of moisture in an air parcel, which is a mixture reflecting different processes. Furthermore, there are currently no observations of SWIs in atmospheric water vapour with high spatial and temporal coverage available on a global scale. For these reasons, numerical models are important in order to disentangle individual effects, study the influence of different processes on the SWI composition during moisture transport and, in the end, improve our understanding of the observed SWI variability.

There exists a large diversity of models, from simple conceptual models to complex isotope-enabled General Circulation Models (GCMs). Idealized process models like the C-G model or Rayleigh distillation provide an interpretative framework to study atmospheric processes like evaporation or rain formation. During the past decades, SWIs have also been added to several GCMs. GCMs simulate isotope physics along the whole pathway of moisture in the atmospheric branch of the hydrological cycle. An overview on modelling SWIs with GCMs can be found in Sturm et al. (2010). Integrating SWIs into models allows for a more detailed diagnostics of the water cycle. Recently, isotope physics have been added to Regional Circulation Models (RCMs) as well (Pfahl et al., 2012; Eckstein et al., 2018). RCMs can be used to study SWI variability of synoptic-scale events. They offer the possibility to investigate the relationship between meteorology and the

spatial isotope distribution. In combination with trajectories, SWI variability and processes influencing the signal along moisture transport pathways can be studied. Furthermore, sensitivity experiments using numerical models allow to differentiate between processes affecting the SWI variability in the atmosphere (Dütsch et al., 2016).

In past years, there were efforts to systematically evaluate isotope-enabled numerical models in the SWI-intercomparison group (Sturm et al., 2010; Risi et al., 2012). However, so far the evaluation most often is restricted to the isotopic composition of precipitation, since data of SWIs in water vapour is still scarce (Galewsky et al., 2016). A GCM showing reasonable model performance when comparing it to measurements from the Global Network of Isotopes in Precipitation (GNIP) is the ECHAM5-wiso (Werner et al., 2011). Furthermore, it also agrees well with SWI vapour data available at several GNIP stations. It is, however, notable that the model evaluation of Werner et al. (2011) was limited to annual, seasonal and monthly timescales. Several shortcomings regarding model performance have been observed by Steen-Larsen et al. (2017) when comparing daily data to output of multiple GCMs. Among the model deficiencies is a poor skill in d-excess over the Greenland Ice Sheet as well as an incorrect simulation of the spatial distribution of SWIs in the MBL of the Northern Atlantic and the Arctic Ocean. Pfahl et al. (2012) compared simulations of the limited-area model $\mathrm{COSMO_{iso}}$ to the measured $\delta^{18}\mathrm{O}$ in vapour and precipitation during a winter storm in North America and showed that the model simulates the temporal evolution of $\delta^{18}\mathrm{O}$ reasonably well. Recent model evaluation of $\mathrm{COSMO_{iso}}$ indicates a good performance with respect to precipitation as well as water vapour in the free troposphere and at the surface on hourly timescales, with only small, temperature dependent biases (Christner et al., 2018). However, this evaluation has been done for Central Europe, a region for which the COSMO model has been originally designed and optimised. The model performance of $\mathrm{COSMO_{iso}}$ in the SO region, which is of interest in the context of this thesis, has not been addressed so far.

1.4 Objectives

In a first step, this thesis combines Antarctic Circumnavigation Expedition (ACE) observations with model simulations in order to assess the performance of the isotope-enabled regional model $COSMO_{iso}$ with respect to meteorology and SWIs in the MBL, near the ocean surface along the ship track of the expedition (Section 2.1). In a second step, model data is used to study moisture transport pathways and the spatial and temporal evolution of SWI variability during two selected case studies (the Mertz and Ross Sea events, see Sections 3.2 and 3.3). Regarding the Ross Sea event, one of the final goals is to disentangle the different processes affecting the MBL isotopic composition of air parcels arriving at the ship's location during an event of strong ocean evaporation. In this thesis, $COSMO_{iso}$ simulations along the first and the second Leg of the ACE track, meaning the South Indian and South Pacific region of the SO, are analysed.
The following research questions are investigated:

1) How well does $COSMO_{iso}$ perform in the MBL in the SO when comparing model output to observations?

2) Which factors affect the model performance?

3) How are SWIs related to environmental conditions during an event of strong ocean evaporation?

4) What is the relative importance of ocean evaporation and MBL mixing for the SWI composition along air parcel trajectories?

The first two research questions will be tackled by combining $COSMO_{iso}$ model simulations with ACE observations. For the second part, concerning the case study, trajectories based on $COSMO_{iso}$ and a trajectory-based box model will additionally be used as tools. These tools will be presented in the upcoming Chapter 2.

Chapter 2

Data and methods

2.1 ACE data

The ACE expedition was an international and interdisciplinary research cruise circumnavigating Antarctica during austral summer 2016/2017. It was organised by the Swiss Polar Institute. The circumnavigation was split into three Legs. Figure 2 shows an overview of the course of the Russian research vessel Akademik Tryoshnikov during the different Legs. The primary focus of this thesis will be on the second Leg, covering the South Pacific sector. Its course proceeds closer to Antarctica compared to the other Legs. While numerous research projects from different scientific disciplines were conducted during ACE, this thesis uses data of the project investigating air-sea interactions in the SO (Project 11, PI Heini Wernli). In-situ measurements of SWIs in water vapour and specific humidity from a Picarro cavity ring-down laser spectrometer L2130 build the basis for evaluation of the $\text{COSMO}_{\text{iso}}$ model with respect to SWIs. Furthermore, micro rain radar data, radio soundings and meteorological ship data (temperature, specific and relative humidity, cloud base height, pressure, wind speed and direction, solar radiation) are available and can be used for model evaluation as well. To assess the model's performance along the ACE Legs 1 and 2 in the MBL, data are compared to model output by, amongst other means, interpolating them along the ship track. In addition, model data and ACE observations are combined with trajectories to study moist atmospheric processes and SWI variability along transport pathways.

Fig. 2. Overview of the ACE expedition. The course as well as well as intermediate stops on SO islands are marked.

2.2 COSMO$_{iso}$

The COSMO model is a limited-area, non-hydrostatic regional atmospheric model. It solves a fully elastic formulation of the governing equations on a numerical grid. While the horizontal discretization is based on standard latitude/longitude grid, a terrain-following vertical coordinate formulation is used. Subgrid-scale processes are represented by parametrisations. Additional information on the dynamics and numerics of the COSMO model can be found in Steppeler et al. (2003). Its design offers flexibility in terms of possible applications: It can be used on a wide range of horizontal resolutions from 50 km down to convection-resolving scales of less than 1 km. COSMO is used operationally for weather forecasting by several national weather services. Besides its use for short- to medium-range forecasts, it can also run in a climate mode to generate regional climate simulations.

Pfahl et al. (2012) included stable water isotopes ($H_2{}^{18}O$ and $HD^{16}O$) into the COSMO model to study the isotopic variability on synoptic scales. The isotope-enabled COSMO version is referred to as $COSMO_{iso}$. In a first case study, they studied the isotopic composition of precipitation of a winter storm in North America. Moreover, they pointed out the possibility to combine $COSMO_{iso}$ with observations on a high temporal resolution.

The basic idea how isotope physics are implemented into $COSMO_{iso}$ follows previous incorporations into numerical atmospheric models (e.g. Joussaume et al., 1984). Parallel to the normal water cycle in the model, a purely diagnostic water cycle is included. To this end, all the prognostic moisture variables are tripled for the heavy isotopologues. The new moisture fields show different behaviour during phase transitions, but are treated the same as the standard moisture variables for all other processes, in particular advection with the large-scale flow, turbulent mixing, and deep convection. Isotopic fluxes related to ocean evaporation are parametrised using the C-G model (Craig and Gordon, 1965). Cloud microphysical processes are affected by fractionation if both the vapour and a condensed phase are involved. Whereas fractionation between cloud droplets and the surrounding air is assumed to be an equilibrium process, for the exchange between rain drops and vapour, kinetic effects are taken into account. During ice deposition, isotopic fractionation is parametrised following Jouzel and Merlivat (1984). Sublimation is, so far, assumed to be a non-fractionating process in the atmosphere as well as at the surface. In this thesis, an updated $COSMO_{iso}$ version assuming equilibrium fractionation during snow sublimation from surface snow is applied as well, closely following Christner et al. (2017). Similarly to the implementation in the cloud microphysical scheme, isotopic fractionation is implemented into the convective cloud scheme whenever phase change takes place. For additional insight regarding the implementation of SWIs into the COSMO model, I refer to Pfahl et al. (2012).

$COSMO_{iso}$ is a limited-area model with its simulation domain only covering a part of the globe. As a consequence, boundary conditions for the standard prognostic variables as well as the additional moisture fields are needed. For this thesis, the initial and boundary values will be provided by the ECHAM5-wiso GCM (Werner et al., 2011). They are available with a spectral resolution of T106 (corresponding to

1.12° at the equator) and 31 vertical levels in a six-hourly temporal resolution. The ECHAM5-wiso GCM is nudged every six hours to surface pressure, temperature, divergence and vorticity of the ERA-40 and ERA-Interim reanalysis datasets (Butzin et al., 2014).

In the context of this thesis, $COSMO_{iso}$ runs will be produced along the first and the second Legs of the ACE ship track. Since the domains for usual COSMO simulations are situated at high latitudes, a standard latitude/longitude grid is not optimal. Thus, the COSMO grids are rotated and new, domain-specific North Poles are defined. The model domains can then be defined on the rotated grids and have a much more isotropic structure. Figure 3 illustrates an example where parallels and meridians are plotted on the globe for both the standard grid as well as for the rotated grid for the first run along Leg 2. Additionally, the domain, defined on the rotated grid, is shown. In order to capture the whole length of Leg 1 and Leg 2 in terms of space and time, the model domains have to be adjusted. In the end, this results in three domains along Leg 1 (Fig. 4) and along Leg 2 (Fig. 5), respectively.

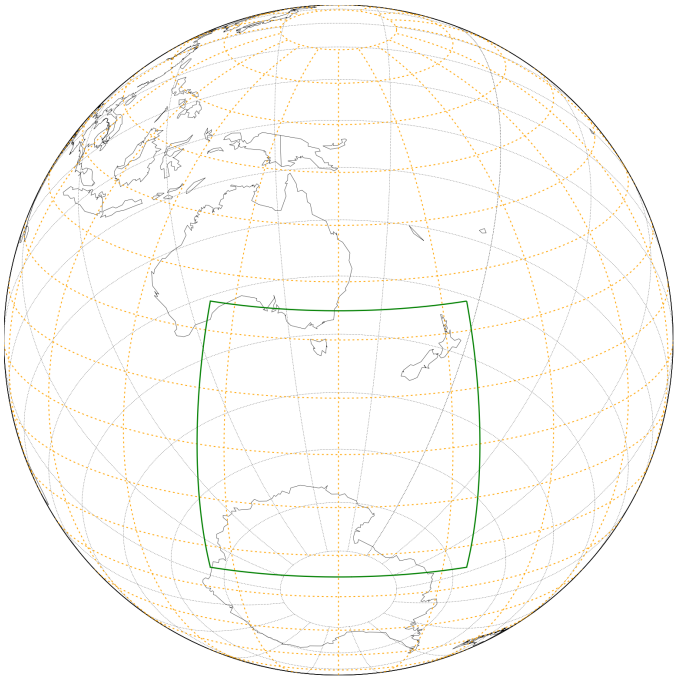

Fig. 3. Illustration of the grid rotation for COSMO simulations. Standard parallels and meridians are shown (in grey) as well as parallels and meridians of a rotated grid (in orange), corresponding to a North Pole situated at 151 °W, 29 °N. Additionally, a domain defined on the rotated grid is shown (in green).

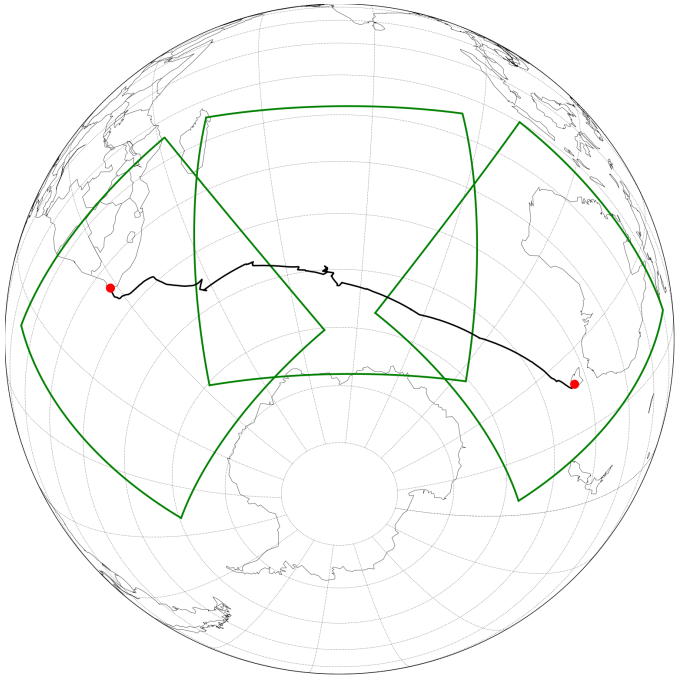

Fig. 4. The three domains along the first Leg of the ACE track. Each of the domains is defined on a different rotated grid.

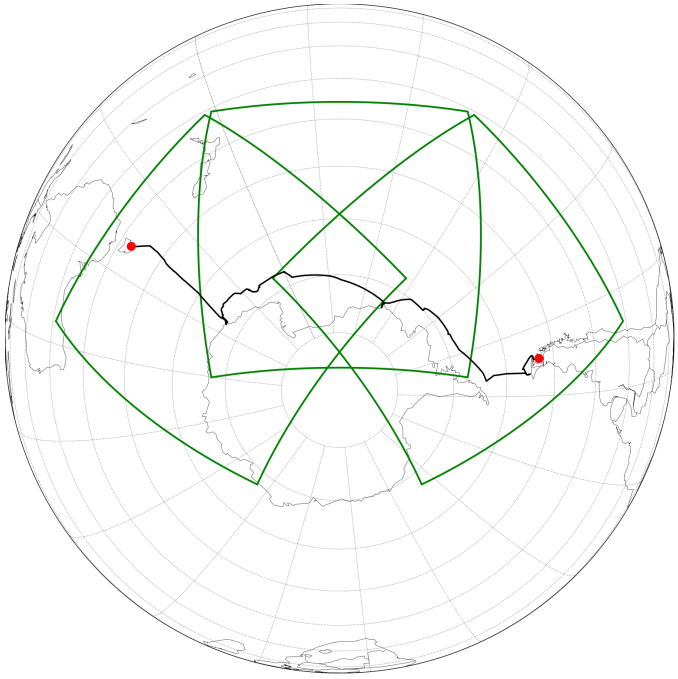

Fig. 5. The same as Fig. 4 but for the second Leg of the ACE track.

The model runs are performed with a horizontal resolution of 0.125°, corresponding to about 14 km grid spacing, and 40 hybrid vertical levels. Initial and boundary fields are taken from the ECHAM5-wiso GCM. The runs are initiated at 13 December 2016 00 UTC, 24 December 2016 00 UTC, 03 January 2017 00 UTC for Leg 1 and 12 January 2017 00 UTC, 28 January 2017 00 UTC, 01 February 2017 00 UTC for Leg 2, respectively, each one of them with an integration time of 720 h. Spectral nudging toward the reanalysis-based dynamical fields of ECHAM5-wiso is applied to the $COSMO_{iso}$ horizontal wind fields above 850 hPa for the large wavelengths (von Storch et al., 2000). The ocean is assumed to have a constant isotopic composition of 1‰ for both heavy isotope species. The simulations are used to study the spatial and temporal evolution of SWIs along Leg 1 and 2, as illustrated for Leg 2 by three different d-excess snapshots in Fig. 6.

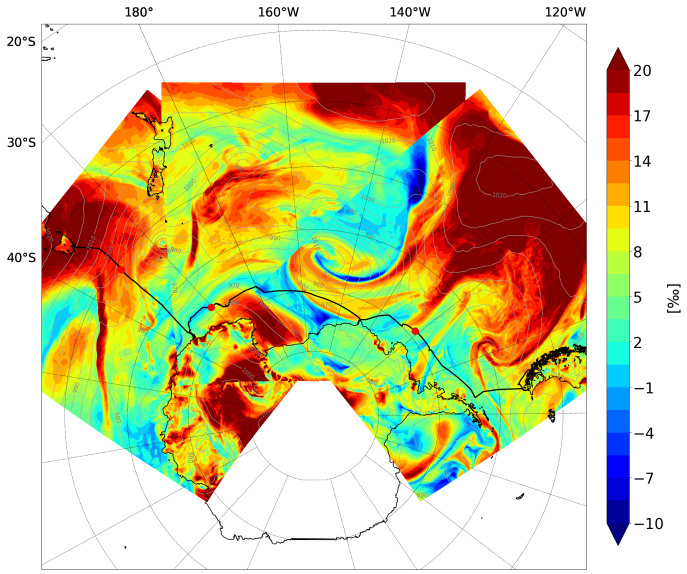

Fig. 6. Visualisation of the model output along Leg 2 (black line). The d-excess in the lowest model level is shown for three different times (24 January 2017 12 UTC, 3 February 2017 00 UTC and 15 February 2017 00 UTC). The ship's position at these times is marked by red circles.

$COSMO_{iso}$ output from the six model runs helps to validate the model using measurements along the ship track, but is also used for a detailed case study including the calculation of backward trajectories and an investigation of the SWI budget and important atmospheric processes that affect the isotopic composition during the transport of air masses. Additionally to the three model runs along both Legs, a run

with doubled horizontal resolution of 0.0625° is performed for the second domain of Leg 2. It delivers information on the added value of modelling SWIs at a higher resolution. Furthermore, the first model simulation along Leg 2 is repeated with the same configuration except adapting the non-equilibrium fractionation factor in order to assess the sensitivity of the near-surface d-excess to the choice of this parameter. Additionally, a run including equilibrium fractionation during surface snow sublimation is included into the performed sensitivity analysis as well.

2.3 Trajectory calculations

Lagrangian studies using trajectories are a frequently used approach to study coherent flow structures in weather systems (Wernli and Davies, 1997). Furthermore, they can be used in order to study processes related to the atmospheric water cycle. Possible applications include the identification of moisture source regions, the investigation of moisture transport pathways and the joint use with observations in order to interpret the SWI composition of precipitation or water vapour (e.g. Sodemann et al., 2008; Aemisegger et al., 2014). The $\text{COSMO}_{\text{iso}}$ wind fields will be used to perform trajectory calculations using the Lagrangian analysis tool LAGRANTO (Wernli and Davies, 1997; Sprenger and Wernli, 2015). LAGRANTO comes along with a wide variety of possibilities for user-defined adjustments, e.g. selecting calculated trajectories based on defined criteria or tracing meteorological variables along the trajectories.

In the context of Section 3.2, which analyses a katabatic wind event on the Antarctic coast at Mertz, 7 day backward trajectories starting in a vertical column above the ACE ship position are calculated in order to interpret the measured SWI signal and the observed model bias. In Section 3.3, an event of strong ocean evaporation is studied in detail. To this end, 7 day backward trajectories are calculated ending in a cylindrical box with 60 vertical levels ranging from the surface up to 700 hPa. The ending points in the Ross Sea are illustrated in Fig. 7. For the box model calculations (see Section 2.4), trajectories ending at 04 February 2017 12 UTC and below 960 hPa are selected.

By tracking changes in the SWI composition of air parcels along trajectories, it

can be investigated how moisture changes affect the isotopic composition and to which processes they are related. The combined approach of observations, model results and trajectories helps to study processes affecting the SWI signals arriving at the ACE research vessel from a Lagrangian point of view, thereby improving our understanding of them and providing a spatial context to the measurements.

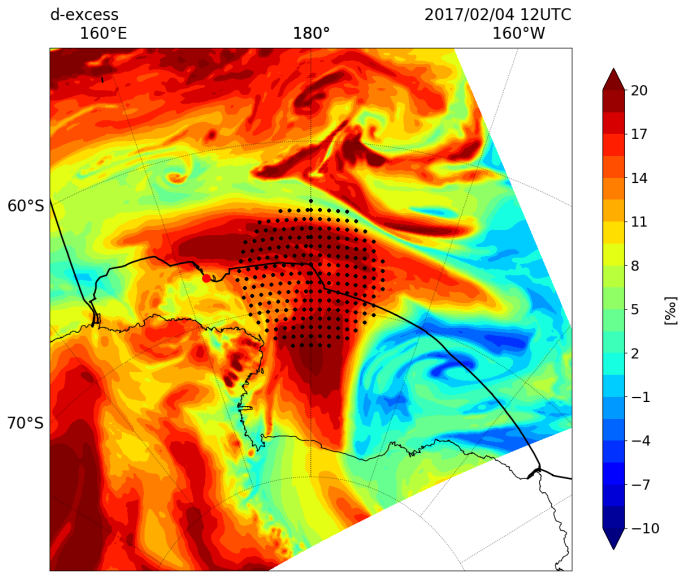

Fig. 7. The coordinates of the ending points of the trajectories for the case study in Section 3.3. Additionally, the d-excess field of the lowest model level is shown for 04 February 2017 12 UTC.

2.4 Isotope budget model along trajectories

The selected case study in Section 3.3 is associated with an event of strong ocean evaporation. For this case, a C-G type of model is applied along the trajectories (Fig. 8).

By iteratively solving the budget equations along the trajectories for the specific humidity as well as the heavy isotopologues, the theoretical isotopic composition of the newly formed vapour from mixing of ocean evaporate with the advected vapour is calculated:

$$Q_i = Q_{i-1} + \Delta Q_i \tag{6}$$

$$Q_i \cdot R^{18}\mathrm{O}_i = Q_{i-1} \cdot R^{18}\mathrm{O}_{i-1} + \Delta Q_i \cdot R^{18}\mathrm{O}_{evap,i} \tag{7}$$

$$Q_i \cdot R^{2}\mathrm{H}_i = Q_{i-1} \cdot R^{2}\mathrm{H}_{i-1} + \Delta Q_i \cdot R^{2}\mathrm{H}_{evap,i} \tag{8}$$

Specific humidity (Q) and its change (ΔQ) are obtained by tracing them along the trajectories. $R^{18}\mathrm{O}_{evap,i}$ and $R^{2}\mathrm{H}_{evap,i}$ are determined following the C-G model, in which $R^{18}\mathrm{O}_{i-1}$ and $R^{2}\mathrm{H}_{i-1}$ serve as input for the advected MBL vapour isotopic composition, either from the previous time step $(i-1)$ or from $\mathrm{COSMO}_{\mathrm{iso}}$ for the initialisation over the continent. The set of equations can then be solved iteratively for $R^{18}\mathrm{O}_i$ and $R^{2}\mathrm{H}_i$.

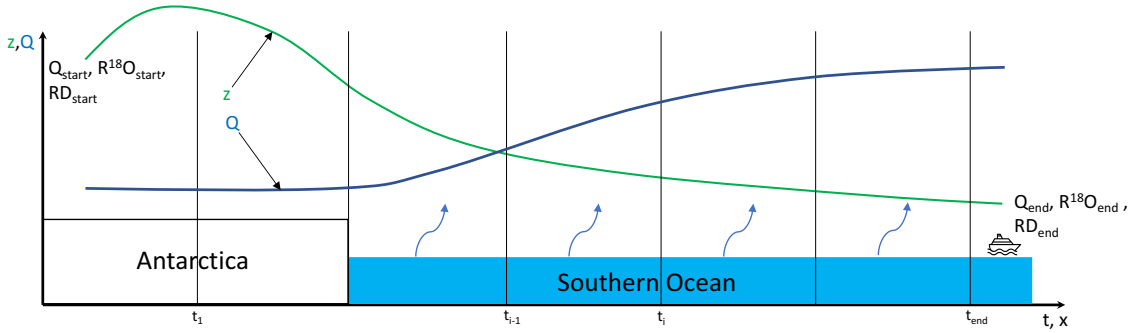

Fig. 8. Illustration of the case study situation where a C-G type of model is used along trajectories. The conceptual pathway of an air parcel originating over Antarctica and subsequently passing over the Ross Sea is indicated (green line). As the air parcel arrives over the ocean, it takes up moisture (blue line) by ocean evaporation (blue arrows). The black vertical lines mark time steps along the trajectory, which are used for the iterative calculation in the budget model.

The shortcomings of the above formulation are that it neglects the influence of turbulent mixing in the MBL and any other subgrid-scale process that can lead to changes in moisture (e.g. condensation, convection). The former is addressed by including an empirical mixing parameter (f_1) into the box model. The humidity budget is adjusted as follows:

$$Q_i = (Q_{i-1} + \Delta Q_{evap,i}) \cdot (1 - f_1) + f_1 \cdot Q_{FT} \tag{9}$$

With Q_{FT} being the free-tropospheric humidity, (9) can be combined with (6) and reformulated in order to obtain the humidity change due to ocean evaporation

($\Delta Q_{evap,i}$), which is needed to calculate the SWI composition according to the C-G equation:

$$\Delta Q_{evap,i} = \frac{\Delta Q_i + f_1 \cdot Q_{i-1} - f_1 \cdot Q_{FT}}{1 - f_1} \tag{10}$$

The isotope budget equations then convert to:

$$R^{18}\mathrm{O}_i = \left(\frac{Q_{i-1} \cdot R^{18}\mathrm{O}_{i-1} + \Delta Q_{evap,i} \cdot R^{18}\mathrm{O}_{evap,i}}{Q_i} \right) \cdot (1 - f_1) + \frac{R^{18}\mathrm{O}_{depleted} \cdot Q_{FT}}{Q_i} \cdot f_1 \tag{11}$$

$$R^{2}\mathrm{H}_i = \left(\frac{Q_{i-1} \cdot R^{2}\mathrm{H}_{i-1} + \Delta Q_{evap,i} \cdot R^{2}\mathrm{H}_{evap,i}}{Q_i} \right) \cdot (1 - f_1) + \frac{R^{2}\mathrm{H}_{depleted} \cdot Q_{FT}}{Q_i} \cdot f_1 \tag{12}$$

(11) and (12) incorporate the process of MBL entrainment into the box model by mixing air with the SWI composition following (7) and (8) with depleted, free-tropospheric air (Q_{FT}, $R^{18}\mathrm{O}_{depleted}$, $R^{2}\mathrm{H}_{depleted}$) according to the entrainment fraction f_1 at each time step. The SWI composition of the depleted air mass and the free-tropospheric humidity is determined upon considering vertical cross sections of $\delta^{18}\mathrm{O}$, $\delta^{2}\mathrm{H}$ and specific humidity (see Fig. 35). The depleted values are set to $R^{18}\mathrm{O}_{depleted} = -40‰$, $R^{2}\mathrm{H}_{depleted} = -290‰$, and $Q_{FT} = 1.0\mathrm{g/kg}$, approximately corresponding to the air at the top of the MBL. Furthermore, the box model is extended by a Lagrangian moisture budget in order to quantify the contributions of the different moisture sources (initial humidity from Antarctica, ocean evaporate, downward mixed humidity from the free troposphere) for the total humidity:

$$Q_{antarctica,i} = Q_{antarctica,i-1} \cdot (1 - f_1) \tag{13}$$

$$Q_{evap,i} = Q_{evap,i-1} \cdot (1 - f_1) + \Delta Q_{evap,i} \cdot (1 - f_1) \tag{14}$$

$$Q_{mixin,i} = Q_{mixin,i-1} \cdot (1 - f_1) + Q_{FT} \cdot f_1 \tag{15}$$

The sensitivity of the box model outcome to MBL mixing is assessed by repeated simulations with a varying f_1 and the results are compared to the simulated isotopic composition of $\mathrm{COSMO_{iso}}$ along the transport pathway. Thereby, the relative importance of evaporation and entrainment into the MBL for the SWI signal in the region of the ship is quantified. Furthermore, the contributions of different moisture sources to the total humidity and their temporal evolution is investigated.

Chapter 3

Results and discussion

3.1 Model validation

This section focuses on the $COSMO_{iso}$ model performance in the MBL in the SO. In a first part, a qualitative validation is done by interpolating meteorological and SWI data along the second Leg and by comparing ACE observations and model output in scatterplots. In a second step, statistical quantities are calculated and presented in the form of Taylor diagrams (Taylor, 2001) in order to characterise the model performance. An intercomparison between $COSMO_{iso}$ and ECHAM5-wiso complements the model validation. In addition, factors influencing the modelled SWI composition are addressed, including the choice of the non-equilibrium fractionation factor in the surface flux parametrisation, the proximity to the Antarctic continent (effect of sea ice, snow-atmosphere interactions) and the quality of the modelled precipitation timing and intensity. The last chapter completes this section by analysing a $COSMO_{iso}$ simulation incorporating equilibrium fractionation during surface snow sublimation.

3.1.1 Interpolated timelines along the ship track for Leg 2

Figure 9 shows the interpolated meteorological variables temperature, specific humidity and relative humidity with respect to sea surface temperature (h_S) along the second Leg. The interpolation of the isotopic variables $\delta^{18}O$, $\delta^{2}H$ and the d-excess is shown in Fig. 10.

Fig. 9. Interpolation of meteorological variables temperature, h_S and specific humidity along the second ACE Leg. The interpolation is shown for the four model runs with the respective colors. Run 4 corresponds to run 2 with a doubled resolution. ACE observations (at five-minutes resolution) are shown in green. The shaded areas represent the uncertainty range.

ACE data at five-minutes temporal resolution are shown as the observational basis, covering a time span from 21 January until 26 February 2017 for the isotope measurements and 22 January until 24 February 2017 for the meteorological ship data. Hourly output of the four $\text{COSMO}_{\text{iso}}$ model runs, in turn, serves as a basis for the modelled timelines obtained from spatial interpolation to the ship's position. Output fields from the lowest model level are used, corresponding to an elevation of about 10 m above sea level, and thus no vertical interpolation is done. This is reasonable since ACE measurements of SWIs and meteorological variables were conducted at 13.5 and 21 m above sea level, respectively. As the ship measurements during ACE are point measurements, it is important to gain some knowledge on the modelled spatial

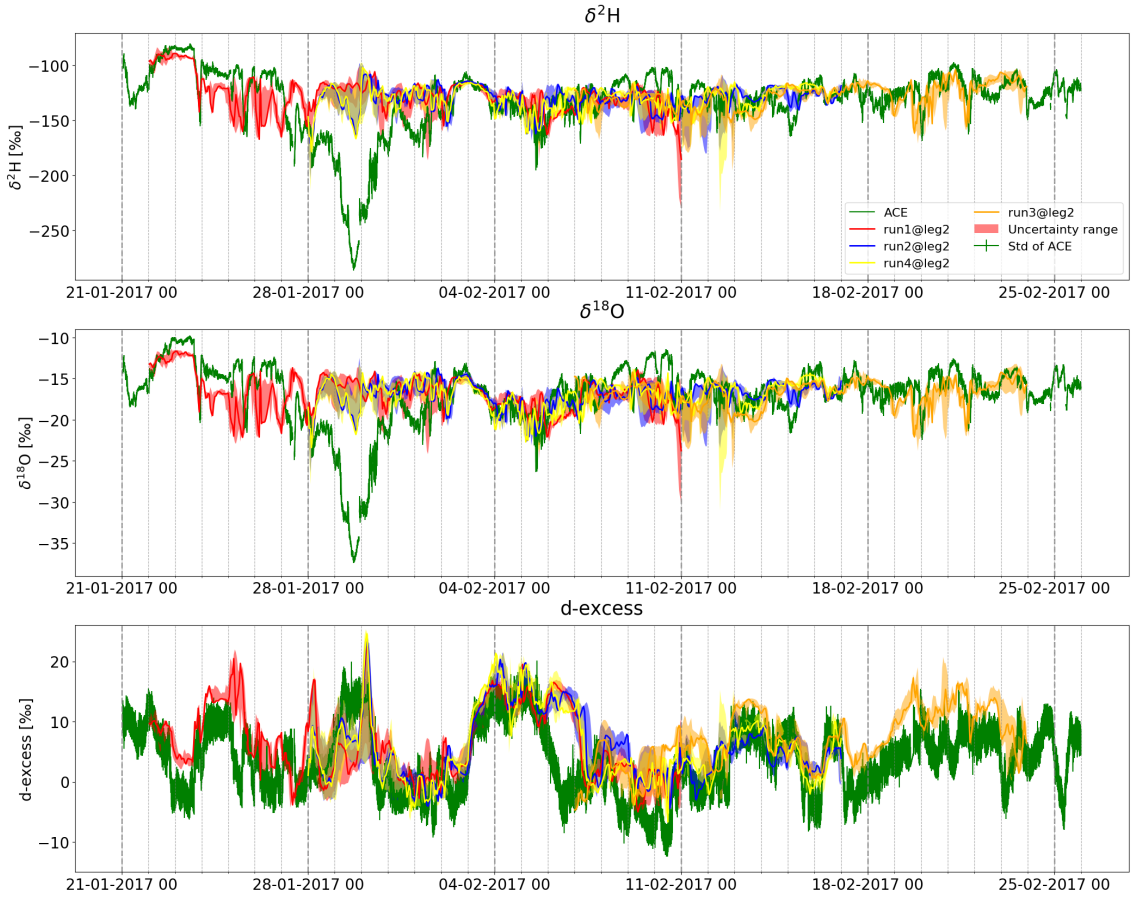

Fig. 10. Same as Fig. 9 but for the isotope variables δ^2H, δ^{18}O and the d-excess.

variability near the ship's position in order to assess the uncertainty associated with the interpolation. To this end, the ship track coordinates are perturbed four times by alternately adding or subtracting 0.5° in latitudinal and longitudinal direction. The lowest and highest values of all interpolations are determined and serve as an empirical uncertainty range.

Overall, measured and modelled temperature and specific humidity are in good agreement (Fig. 9). The meridional gradient in the beginning and at the end of the Leg is well captured by the model. The observed variability on daily timescales is generally well represented apart from the strong temperature and humidity drop around 29 January 12 UTC. Modelled temperature and humidity are both too high during this event. Regarding h_S, the general agreement between the model and the observations is less good. Nevertheless, the majority of sub-weekly to daily variability is captured by the model. The uncertainty range associated with h_S

is larger than for temperature and specific humidity. This is in accordance with short-term fluctuations being more prevalent in both measurements and modelled values of h_S.

The overall correlation between observed and modelled SWIs is good as well but less pronounced than for temperature and specific humidity (Fig. 10). The agreement shows a high temporal variability, leading to a substantially varying performance for different events. Daily variability is, to some extent, better represented for the d-excess than for $\delta^{18}O$ and $\delta^{2}H$. However, d-excess values in the model are systematically biased towards higher values.

A striking feature is the event at the end of January, where exceptionally low values were measured for $\delta^{18}O$ and $\delta^{2}H$. This event has not been captured by the model at all, neither in terms of SWI signals nor by the meteorological parameters. The vessel was situated at the Mertz glacier in proximity to the coast of Antarctica during this time span. This event (hereafter referred to as Mertz event) will be analysed in more detail in Section 3.2.

Another extraordinary event to highlight is the episode from 03 February 00 UTC to 06 February 12 UTC. During this time period, the observed d-excess was exceptionally large. The onset and magnitude of the event are represented well in the model, though the high d-excess values persisted for longer than indicated by the observations. This event (hereafter referred to as the Ross sea event) will be subject to a detailed case study in Section 3.3.

In summary, this first model assessment, based on the comparison of timelines, indicates an overall satisfying performance of $\text{COSMO}_{\text{iso}}$ in the SO. Meteorological conditions are better represented by $\text{COSMO}_{\text{iso}}$ than the SWI variability. This result does not change when using a higher horizontal model resolution. A doubling of the horizontal resolution (0.0625° instead of 0.125°) does not increase the agreement between $\text{COSMO}_{\text{iso}}$ and the observations (see run 4 in Fig. 9 and 10)

3.1.2 Comparison of ACE and COSMO$_{iso}$ data for Leg 2

Scatterplots of observations and interpolated model values at the ship's position are an additional possibility do display the model performance. In the following, this is done for the second Leg and for each joint tuples of observation and model values.

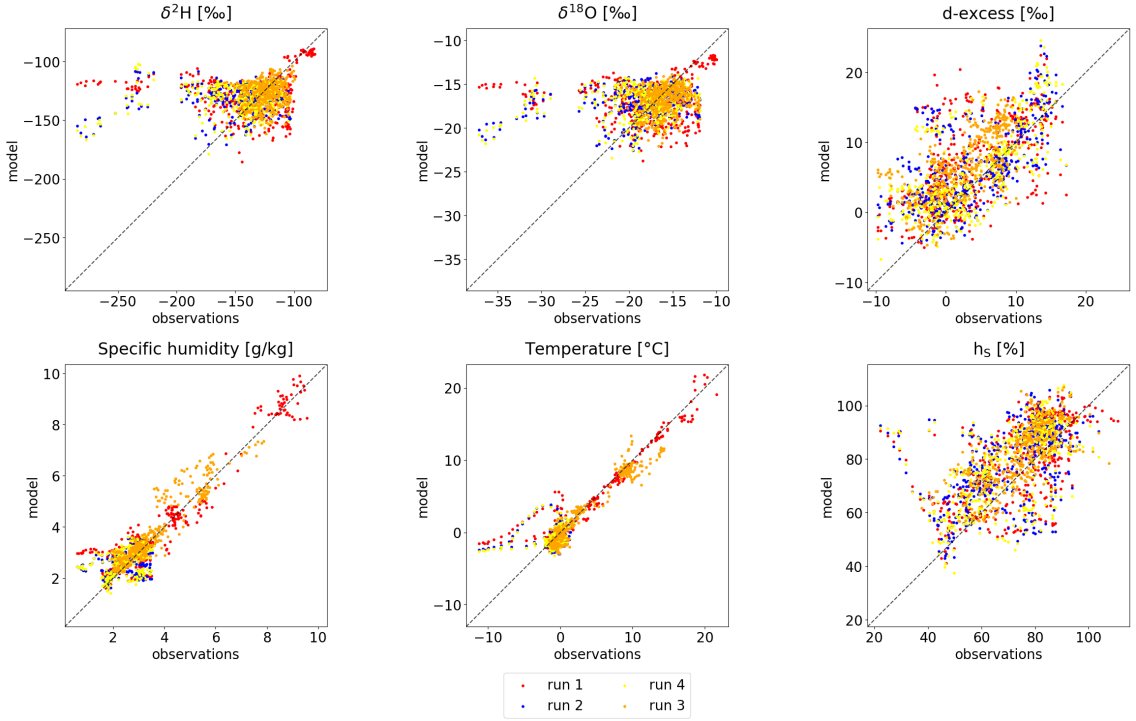

Fig. 11. Scatterplots of observations and interpolated model data. Hourly COSMO$_{iso}$ data and the corresponding five-minutes ACE observations are used for the interpolation. The different model runs are indicated by different colors. Additionally, the 1:1 line is shown as a reference.

Figure 11 shows scatterplots of the meteorological variables and the SWI composition of water vapour for the second Leg. This additional representation of the model performance confirms the analysis from the previous subsection. For temperature and specific humidity, the pattern shows the smallest spread and the majority of the points align along the 1:1 line. For h_S and the isotope variables, the distribution of the data points is still systematically oriented along the reference diagonal, however the spread is much larger. The d-excess shows again a positive systematic bias. Modelled temperature and δ-variables differ most for the Mertz event, with values systematically larger than observed.

After the qualitative assessment, a quantitative analysis of the model performance is presented. To this end, the following statistical measures are used: The standard deviation (s_x), the centered root mean squared error ($RMSE$) and the Pearson correlation (ρ).

$$s_x = \sqrt{\frac{\sum_{i=1}^{N}(x_i - \bar{x})^2}{N-1}} \tag{16}$$

$$RMSE = \sqrt{\frac{\sum_{i=1}^{N}\Big((m_i - \bar{m}) - (o_i - \bar{o})\Big)}{N}} \tag{17}$$

$$\rho = \frac{\sum_{i=1}^{N}(m_i - \bar{m}) \cdot (o_i - \bar{o})}{N \cdot s_m \cdot s_o} \tag{18}$$

While s_x is used for both observations and model values separately, m stands for model data, o for observations and N is the number of data points (overbars denoting mean values of the respective quantities). In combination, these different scores can give a broad overview on different aspects of the model performance. They deliver information about the modelled and observed variability, the mean model error and the temporal correlation between model and observations. The three quantities are displayed in Taylor diagrams in Fig. 12 and 13.

Temperature and specific humidity show high correlations for run 1 and 3 (> 0.93) and lower values for run 2 (0.5 for specific humidity, 0.25 for temperature). For these variables, observed and modelled standard deviations are very similar for run 1 and 3, while modelled variability is too low during run 2. The $RMSE$ is low for specific humidity (0.4–0.6 g/kg) and temperature (< 2 °C). h_S shows a similar model performance over all runs: Correlation values are in the range of 0.6–0.7, observed and modelled variabilities agree well and the $RMSE$ is < 15‰ for all runs.

Correlations are low for the δ-variables (< 0.3) and higher for the d-excess (> 0.6). While the standard deviation of model and observations are similar for the d-excess, modelled standard deviation is substantially smaller than observed for the δ-variables for run 1 and 2. This is an effect of the Mertz event, during which the SWI composition of the vapour was exceptionally depleted. Therefore, the observations

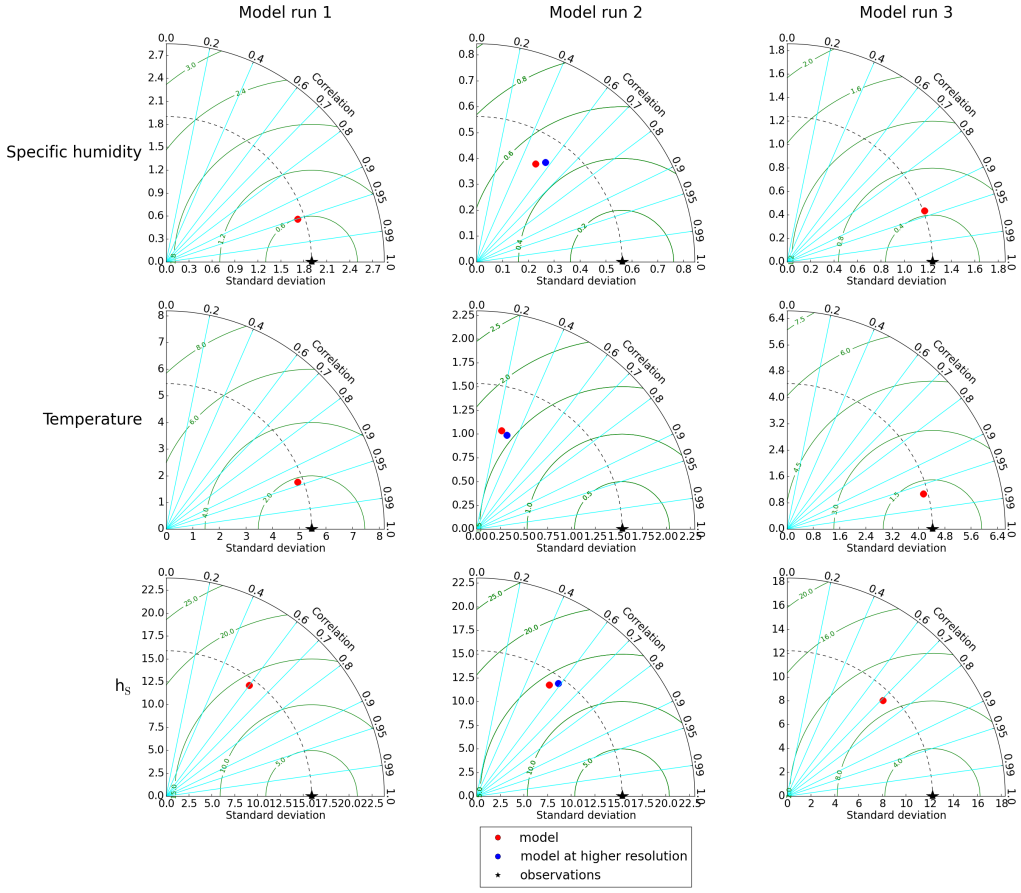

Fig. 12. Taylor diagrams for the meteorological variables specific humidity, temperature and h_S. Shown are diagrams for all model runs. Model run 4 (model run at higher resolution) is compared to the same observational period as model run 2 and is thus plotted into the same diagrams (in blue). While the radial axes serve to compare standard deviation of observations and the model (standard deviation of observations is indicated by the dashed line), the inclined axes show the correlation (blue contour lines) and the $RMSE$ is added by green contour lines.

include a larger range of values compared to the model timeseries, consequently leading to a larger standard deviation in the measurements. The $RMSE$ for the d-excess is rather small (< 5.5‰). For the δ-variables, the $RMSE$ is large for run 1 and 2 (32–38‰ for δ^2H, 4.2–5.2‰ for δ^{18}O) but lower for run 3 (15‰ for δ^2H and 2‰ for δ^{18}O). This is a consequence of the $RMSE$ accounting for the too enriched $\text{COSMO}_{\text{iso}}$ δ-values during the Mertz event in run 1 and 2.

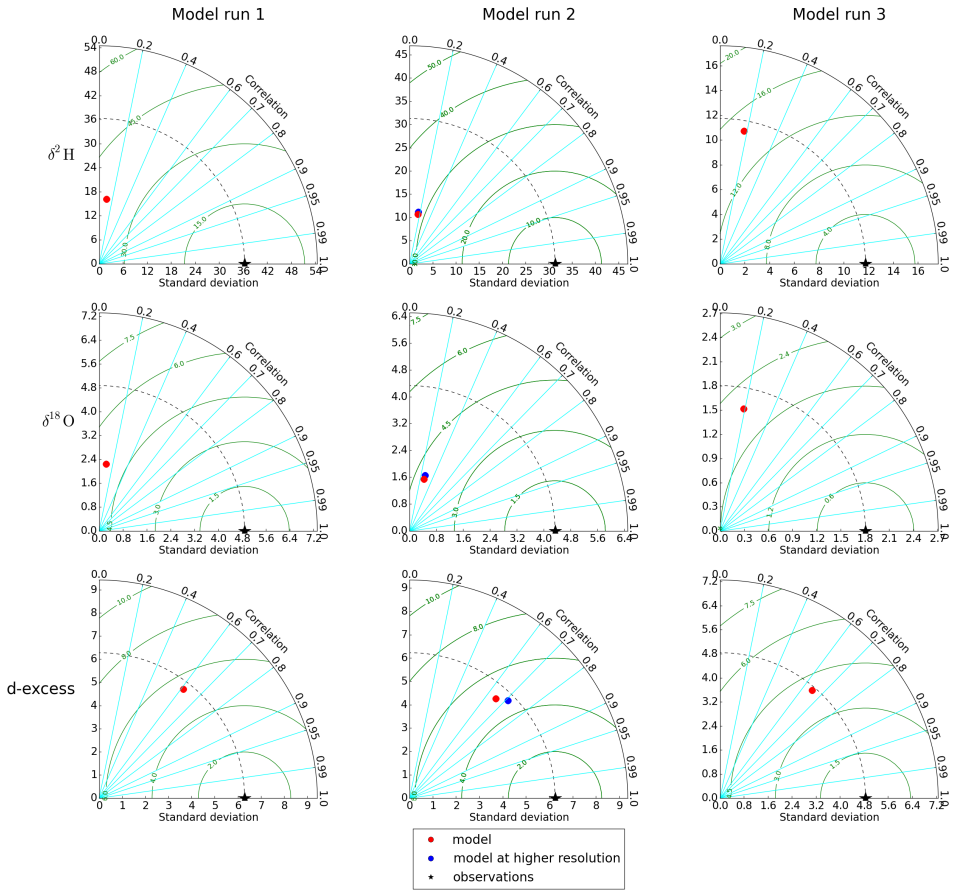

Fig. 13. Same as Fig. 12 but for the isotopic variables δ^2H, δ^{18}O and the d-excess.

The blue dots in Fig. 12 and 13 represent the model run 4 with doubled resolution. For the meteorological variables and the d-excess, correlation slightly increases, while it is virtually the same for the δ-variables. Overall, the differences are small, either indicating that horizontal model resolution is not a major factor limiting model performance, or that it was not increased enough for a more realistic representation of the steep Antarctic coastlines and their impact on the low-level flow.

The statistical scores confirm the previous findings: Meteorological variables are better captured by the model than the SWI composition. The reason for a decreased model quality with respect to meteorological variables for run 2 is in accordance with the fact that this period does, in contrast to run 1 and 3, not include any meridional gradient. Therefore, daily variability, which is less well captured by $\text{COSMO}_{\text{iso}}$, stands out more during run 2. The d-excess is better represented than δ^{18}O and

δ^2H. Run 3 is the only run which does not cover the time period of the Mertz event. Therefore, it outperforms the other runs with respect to the SWI signals. The added value of a doubled horizontal resolution is small. The statistical assessment indicates an overall intermediate model performance and points towards several model deficiencies. Possible explanations for the difficulty of the model to capture fluctuations on short temporal and small spatial scales and the large spread in the isotope variables will be addressed in subsequent chapters. They include:

- Missing representation of isotopic fractionation during ice- and snow-atmosphere interactions preconditioning air parcels before their advection over the open ocean
- An oversimplified treatment of sea ice and its effect on surface fluxes
- Neglecting the effect of sea spray on the SWI composition near the surface in the MBL
- Deficiencies with respect to the parametrisation of boundary layer turbulence
- Errors in the initial and boundary data
- Model shortcomings with respect to the timing and intensity of precipitation affecting the boundary layer vapour through below-cloud interactions with falling hydrometeors

Despite these potential shortcomings, the model can still be used for process studies focusing on events which were captured well in terms of the timing and characteristics of large-scale weather systems. One such an example is the Ross Sea event, which will be discussed in detail in Section 3.3.

3.1.3 Comparison of ACE and ECHAM5-wiso data for Leg 2

Motivated by the previous subsections comparing ACE observations to $\text{COSMO}_{\text{iso}}$ model data, this chapter complements the validation by an additional comparison of the observations with the ECHAM5-wiso GCM data. To this end, Fig. 14 and 15 show six-hourly ECHAM5-wiso output of meteorological and SWI variables interpolated along the second Leg, respectively. Again, the lowest model level is used

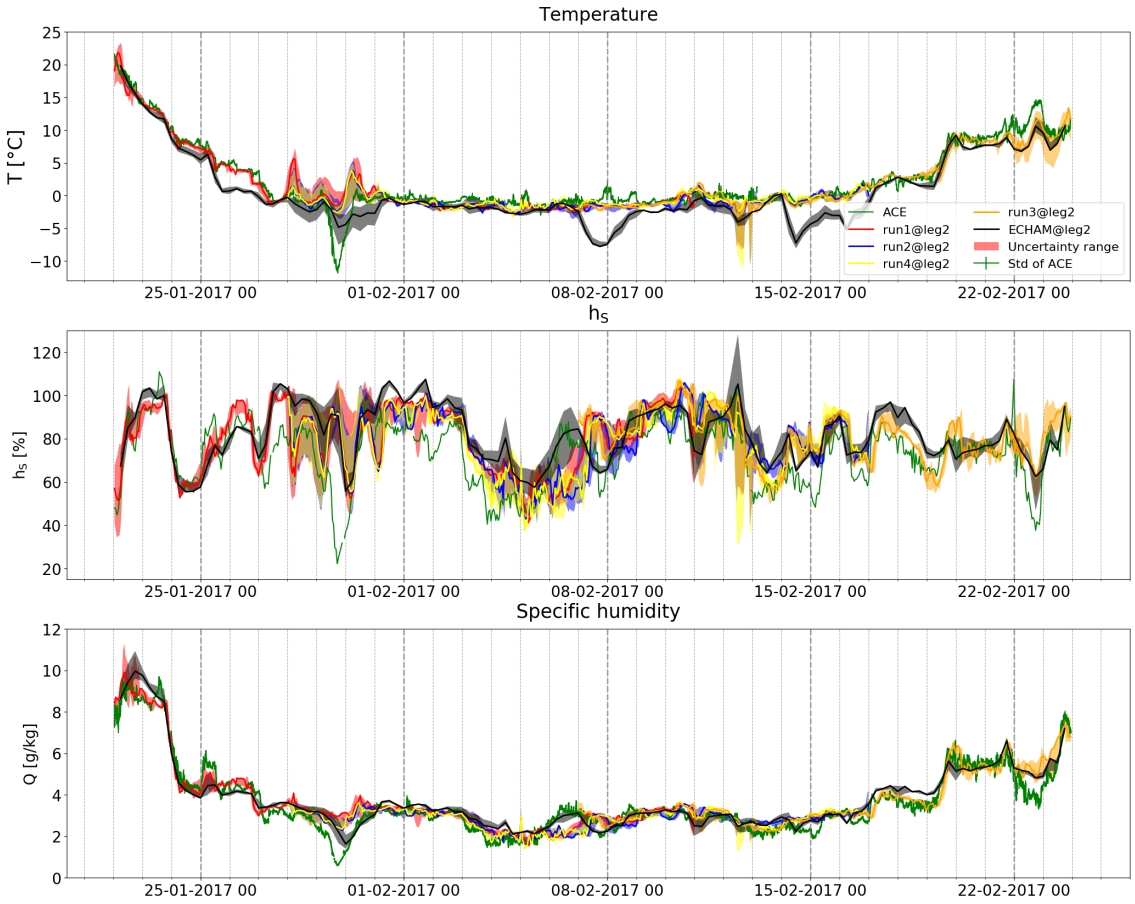

Fig. 14. Same as Fig. 9. Additionally to $\text{COSMO}_{\text{iso}}$, interpolated ECHAM5-wiso data is shown (black lines).

for the interpolation. Figure 16, in turn, adds tuples of six-hourly ECHAM5-wiso data to the five-minutes ACE observations in the scatterplots.

As visible from the timeseries (Fig. 14) as well as the scatterplots (Fig. 16), the ECHAM5-wiso performance with respect to the meterological parameters is comparable to $\text{COSMO}_{\text{iso}}$. This similarity in the performance is seen in the statistical scores as well (see in Fig. A1). There are small systematic biases in the ECHAM5-wiso GCM data compared to the observations. While specific humidity and h_S are systematically shifted towards higher values in the model, there is a cold temperature bias in the GCM compared to observed values.

Changing the focus towards SWI variables (Fig. 15 and 16), ECHAM5-wiso clearly differs from $\text{COSMO}_{\text{iso}}$. Two contrasting observations arise regarding the model

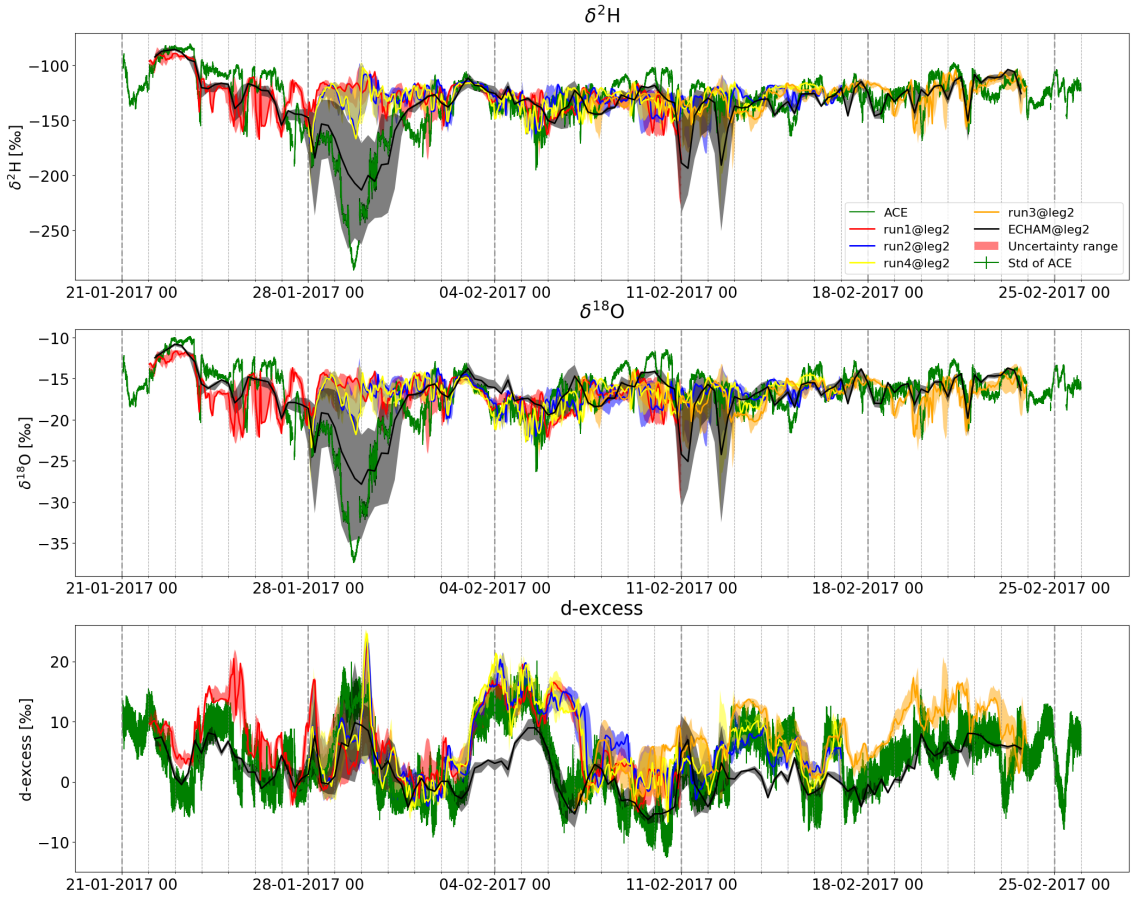

Fig. 15. Same as Fig. 14 but for the isotope variables δ^2H, δ^{18}O and the d-excess.

performance. On the one hand, d-excess model variability is too small compared to observed variability. Especially events linked to high d-excess (e.g. the Ross sea event lasting from 03 February 00 UTC until 06 February 12 UTC) are not as well represented in ECHAM5-wiso as they are in $\text{COSMO}_{\text{iso}}$. On the other hand, ECHAM5-wiso performs well with respect to δ^{18}O and δ^2H. Due to its coarse temporal resolution, fluctuations on very short timescales are not represented. Nevertheless, the model is able to represent variability on daily timescales. In particular, the SWI drop during the Mertz event (end of January) seems to be better captured by the ECHAM5-wiso than by $\text{COSMO}_{\text{iso}}$. This observation is also reflected in the substantially higher correlation values for the δ-variables (> 0.78) compared to $\text{COSMO}_{\text{iso}}$ (< 0.3). The large difference in correlation between the models is reasonable since the magnitude of the overall variability during Leg 2 is dominated by the Mertz event.

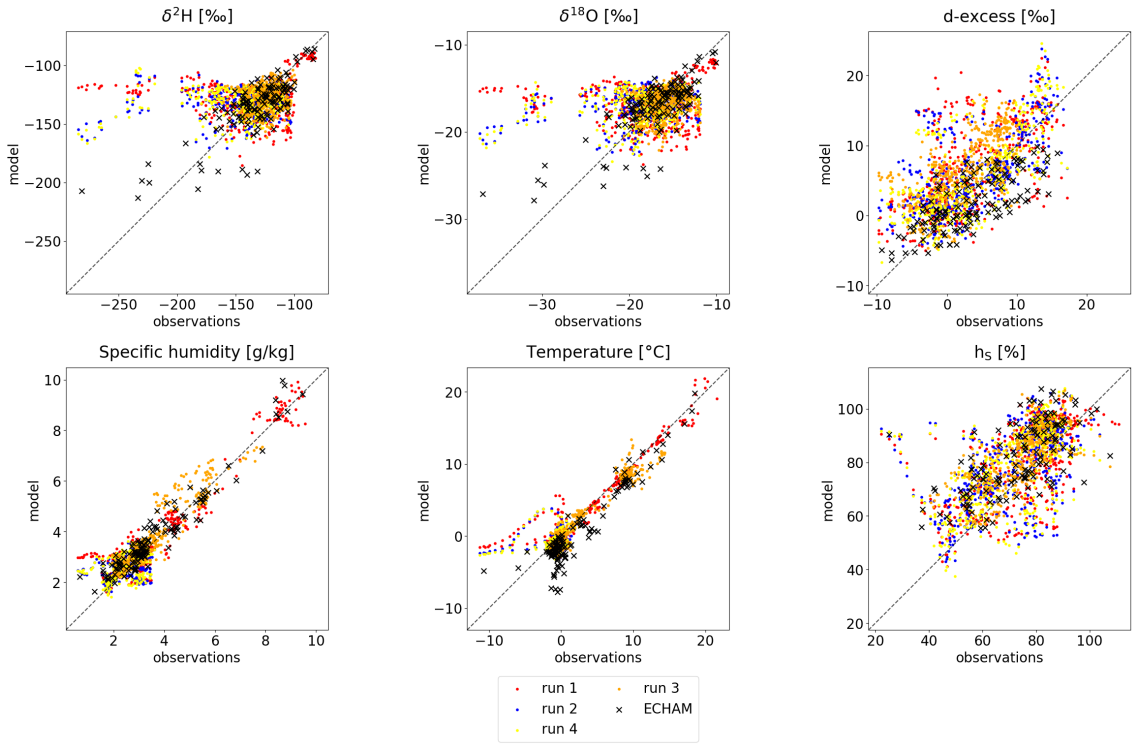

Fig. 16. Same as Fig. 11. Additionally to $\text{COSMO}_{\text{iso}}$, six-hourly ECHAM5-wiso and the corresponding five-minutes ACE observations are shown (black).

Even though modelled values agree better with observations during the Mertz event, this does not necessarily imply that the underlying dynamics are captured better by ECHAM5-wiso. Figure 17 shows δ^{18}O values averaged at each grid point of the lowest model level over the three different model runs for $\text{COSMO}_{\text{iso}}$ (left panel) and over the corresponding period for ECHAM5-wiso (right panel). While the SWI composition is similar over ocean regions, it differs strongly over Antarctica between the two models. δ^{18}O values in $\text{COSMO}_{\text{iso}}$ are much higher and show a more variable pattern, whereas δ^{18}O shows low values in ECHAM5-wiso along the Antarctic coastline and reaches values below -80‰ in the interior of the continent. As a consequence, interpolated δ-values in ECHAM5-wiso always drop if the ship approaches Antarctica. This argument is supported by the fact that interpolated ECHAM5-wiso δ-values show two additional minima around 11 February 06 UTC and 12 February 12 UTC (Fig. 15). These two minima, which were not observed during ACE, coincide with a time period when the ship was positioned close to the Antarctic coastline. Therefore, the superior representation of the strongly depleted air masses in the interior of Antarctica

in ECHAM5-wiso leads to a better correlation with SWI measurements during ACE.

Erroneous initial and boundary data is thus not the main reason for the mismatch between $COSMO_{iso}$ and ACE δ-values. Instead, it is likely that $COSMO_{iso}$ has deficiencies in simulating isotopic distillation during meridional moisture transport and/or the lack of isotopic fractionation during ice-atmosphere and snow-atmosphere interactions is responsible for the observed model shortcomings.

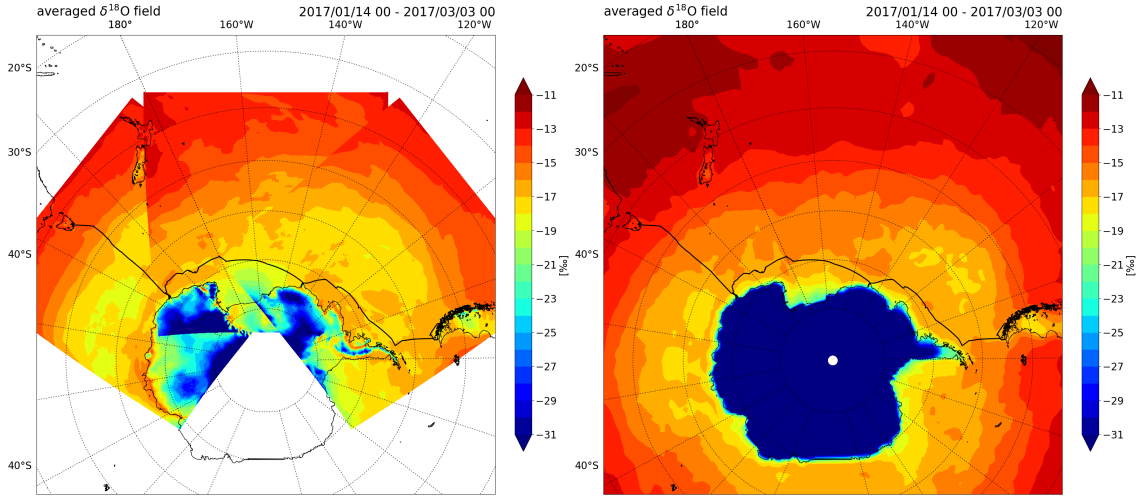

Fig. 17. Averaged output fields of the lowest model level. Left panel: $COSMO_{iso}$, for each run, the whole time span except the first 2 days is taken into account; Right panel: ECHAM5-wiso, from 14 January until 03 March.

3.1.4 Sensitivity of $COSMO_{iso}$ to the choice of the non-equilibrium fractionation factor

In $COSMO_{iso}$, the isotopic composition of ocean evaporate is calculated with a C-G type of model (see Section 1.2). This type of parametrisation prescribes non-equilibrium effects with the aid of the non-equilibrium fractionation factor (α_k), defined as:

$$\alpha_k = \left(\frac{D}{D'}\right)^m \tag{19}$$

This definition accounts for the differing diffusivities of the isotopologues by the ratio of the diffusion coefficents (D and D') as well as the flow regime via the exponent (m). In most of the isotope-enabled GCMs, a wind-dependent formulation

of α_k following Merlivat and Jouzel (1979) is incorporated (e.g. Sturm et al., 2010). Simulations with $\text{COSMO}_{\text{iso}}$ performed during this thesis, however, used a wind-independent formulation after Pfahl and Wernli (2009) with $m = 0.28$. This formulation has shown to perform well in the Mediterranean (Pfahl and Wernli, 2009). However, it still has to be determined whether this parametrisation is the best choice for the SO region as well. Motivated by the systematic positive bias of the d-excess (Fig. 11), this subsection elaborates on the sensitivity of the d-excess in the MBL in the SO with respect to the choice of the non-equilibrium fractionation factor. To this end, an additional $\text{COSMO}_{\text{iso}}$ run was performed with $m = 0.218$ after Merlivat and Jouzel (1979) for $\mid U \mid^{10\text{m}} = 6$ m s^{-1}. Apart from α_k, the same model setup was used as for run 1. This run is referred to as run 1_{MJCW}.

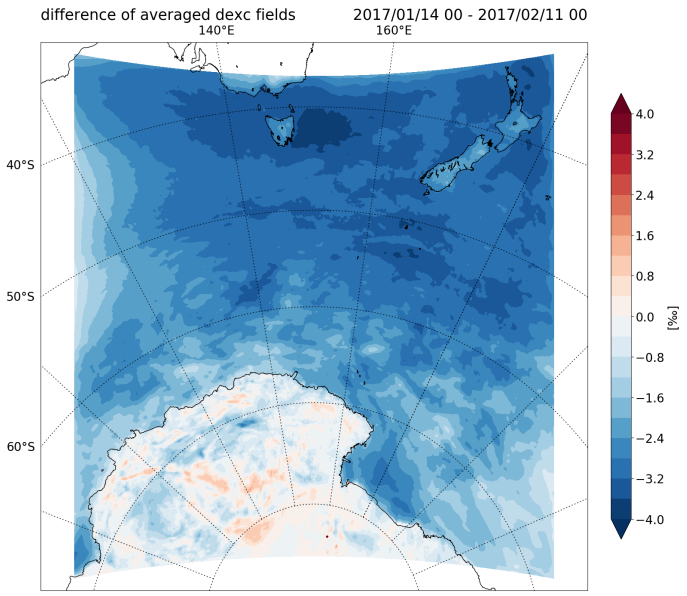

Fig. 18. Difference of averaged d-excess values at each grid point at the lowest model level for run 1 and run 1_{MJCW} (i.e. run 1_{MJCW} − run 1).

Figure 18 illustrates that mean differences between run 1 and run 1_{MJCW} are small over the Antarctic continent, but substantial over the ocean. The overall mean difference between both runs is 2‰. The spatial pattern is rather homogeneous, apart from a minor increase towards lower latitudes. This pseudo-climatological view indicates a lower d-excess if α_k is chosen according to Merlivat and Jouzel (1979) for $\mid U \mid^{10\text{m}} = 6$ m s^{-1}.

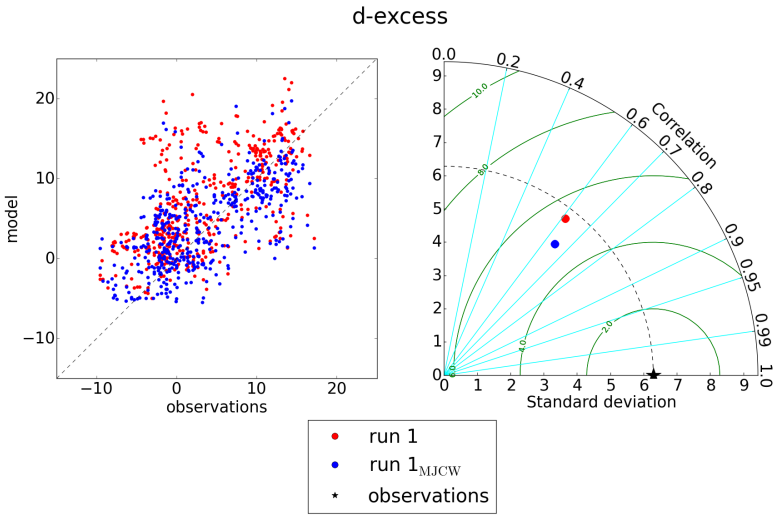

Fig. 19. Left side: Scatterplot of observations and interpolated model data. Hourly $\text{COSMO}_{\text{iso}}$ data and the corresponding five-minutes ACE observations are used for the interpolation. The different model runs are indicated with different colors; Right side: Taylor diagram of the d-excess for both runs.

After having considered the pseudo-climatological perspective, Fig. 19 compares the model performance of the different runs. There is a shift of modelled d-excess towards lower values for run 1_{MJCW} along Leg 2 (blue dots in Fig. 19), especially for high d-excess values. This is in agreement with the pseudo-climatological pattern. The statistical scores, however, do not indicate a clear improvement. On the one hand, correlation is slightly larger and the $RMSE$ smaller. On the other hand, the modelled standard deviation decreases compared to the observations, indicating a reduced variability in the near-surface d-excess. In summary, this sensitivity study indicates possible improvements in modelling d-excess by adapting α_k, but the exact value in order to best match observations in the SO and the potential role of other processes such as turbulent mixing for boundary layer d-excess signals have yet to be determined in future studies.

3.1.5 $\text{COSMO}_{\text{iso}}$ runs along Leg 1

The primary model evaluation using ACE observations along the second Leg showed a decrease in model performance when approaching Antarctica. In addition, the evaluation of ECHAM5-wiso data pointed out possible model deficiencies related to fractionation during ice- and snow-atmosphere interactions. These results indicate

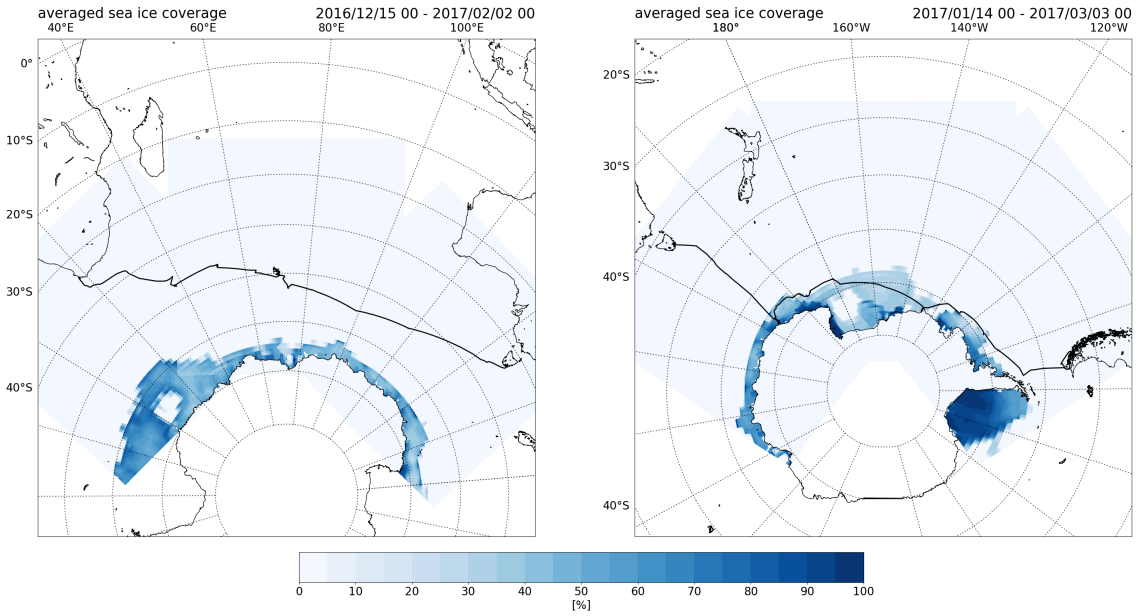

Fig. 20. Ship track (black line) of Leg 1 (left panel) and Leg 2 (right panel). Color shading indicates the average sea ice coverage at each surface grid point. For each run the whole time period except for the first 2 days is considered.

a dependence of the model performance on the proximity to Antarctica, where the influence of air masses advected from the interior of the continent is important. Furthermore, the model performance might decrease in areas with a frequent sea ice coverage, where the simplified sea ice treatment in $\text{COSMO}_{\text{iso}}$ affects air-sea interactions and thus also surface isotopic fluxes. In order to assess if the difficulties are related to the proximity to Antarctica, the following subsection addresses the model performance of $\text{COSMO}_{\text{iso}}$ runs along the first Leg in the mid-latitude SO and compares them to the second Leg. The characteristics of Leg 1 clearly differ from Leg 2, which is illustrated in Fig. 20. Leg 2 includes meridional passages in the beginning and the end, while staying close to Antarctica in between. The average sea ice coverage in Fig. 20 reveals that $\text{COSMO}_{\text{iso}}$ simulates sea ice at the ship's position during a substantial time period along Leg 2. Leg 1, on the other hand, proceeds more zonally and in larger distance to the Antarctic continent. No sea ice is present in $\text{COSMO}_{\text{iso}}$ along the first Leg. Therefore, the influence of Antarctic air mass advection and sea ice are expected to be more important for Leg 2 than Leg 1.

To evaluate the model for Leg 1, the same methods are used as before. Figure 21

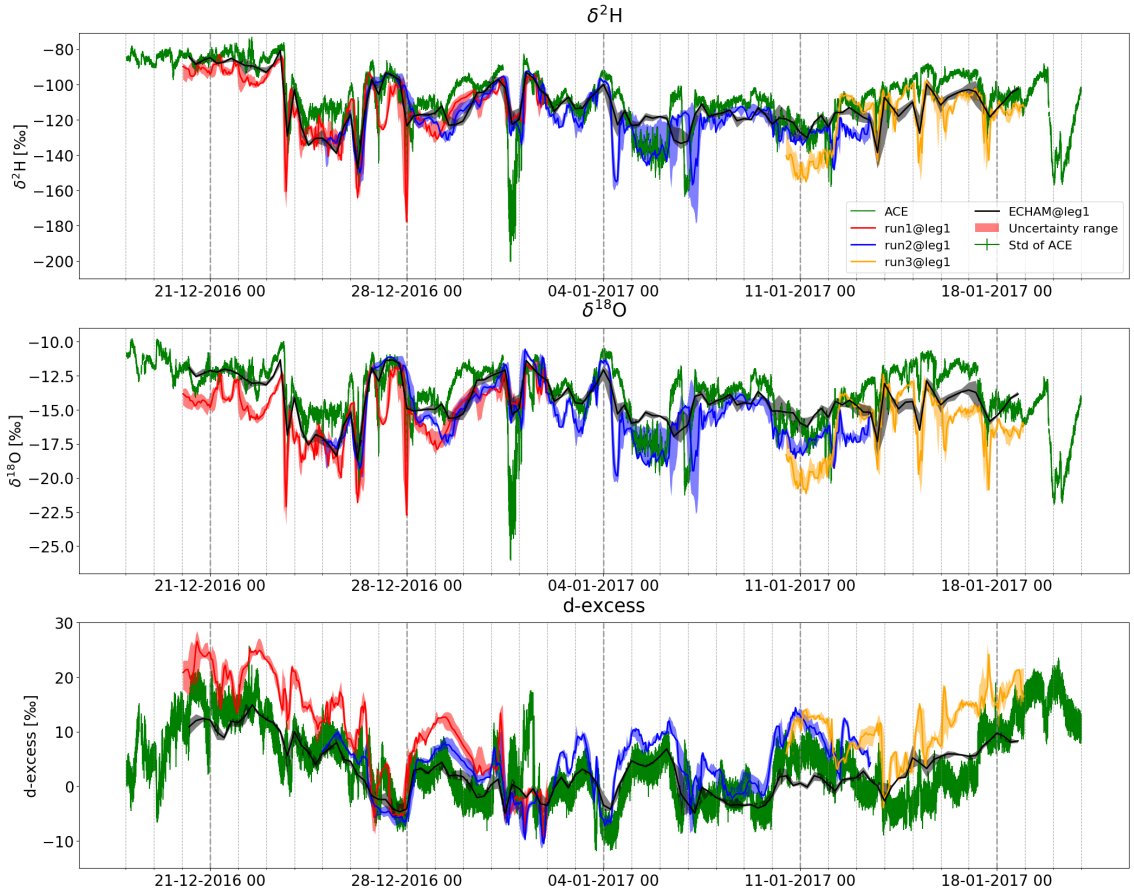

Fig. 21. Same as Fig. 15 but for Leg 1.

shows SWI variables of $COSMO_{iso}$ and ECHAM5-wiso, interpolated along the first Leg of ACE. Additionally, Fig. 22 shows scatterplots of observed and modelled values.

As visible in Fig. 21 and 22, $COSMO_{iso}$ performs better along the first Leg compared to the second Leg with respect to SWIs. Fluctuations on short timescales during the passage of weather systems are well captured, although their magnitude is often over- or underestimated. This improvement compared to Leg 2 is also reflected in increased correlation values of 0.6–0.7 for the δ-variables and 0.5–0.8 for the d-excess (see in Fig. A2). These values are comparable to the correlations of ACE observations with ECHAM5-wiso along Leg 1 (see in Fig. A4). While $COSMO_{iso}$ tends to overestimate SWI-variability, modelled standard deviation in ECHAM5-wiso is too small. It is noteworthy that systematic biases exist for the SWI variables: $COSMO_{iso}$ underestimates $\delta^{18}O$ and $\delta^{2}H$ values and overestimates

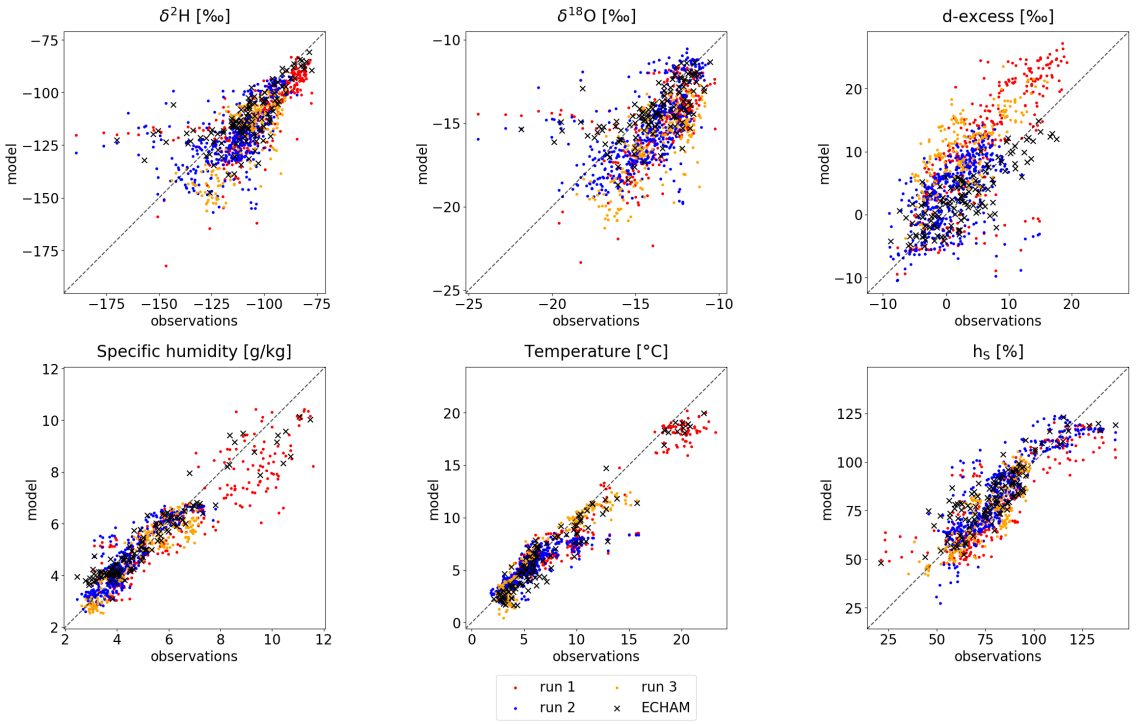

Fig. 22. Same as Fig. 16 but for Leg 1.

d-excess, especially for high values associated with elevated ocean evaporation during the beginning and the end of Leg 1 (see in Fig. A5). The bias is likely related to the non-equilibrium fractionation factor chosen in the model setup for the simulations along Leg 1 (see Subsection 3.1.4). This is in agreement with a recent study by Aemisegger and Sjolte (2018) showing a positive bias for d-excess in evaporation when using α_k following Pfahl and Wernli (2009). ECHAM5-wiso likewise shows some bias towards too low δ-values. For the d-excess, on the other hand, ECHAM5-wiso underestimates the events where high values are reached, similarly to Leg 2. This, in turn, might be due to the use of a wind-dependent non-equilibrium fractionation factor.

Considering meteorological variables, the model performance of Leg 1 and Leg 2 is comparable. Correlation values are similar for specific humidity and temperature and larger for Leg 1 than Leg 2 for h_S. This applies for both ECHAM5-wiso (see Fig. A3, A1 and A4) and $\text{COSMO}_{\text{iso}}$ (see Fig. 12 and A6).

This model evaluation along Leg 1 confirms the proposed explanation for the model

deficiencies along Leg 2. While the model performance with respect to meteorology is similar to Leg 2, the ability of $COSMO_{iso}$ to represent SWI variability in the MBL increases over the open ocean, where the influence of Antarctic air masses and sea ice is small. The observed signal is rather governed by ocean evaporation and the passage of mid-latitude weather systems along Leg 1. Thus, this comparison gives useful information on the reasons for the observed model deficiencies, namely the neglected fractionation effects during snow-atmosphere interactions.

3.1.6 The effect of precipitation on model performance

Another aspect which might influence the performance of $COSMO_{iso}$ with respect to SWIs, is the effect of precipitation. Below-cloud rain evaporation is known to affect the isotopic composition of both precipitation and the surrounding vapour (Dansgaard, 1964; Gat, 1996; Graf et al., 2019). During the evaporation of droplets, the depleted isotopic composition of the evaporate with respect to the ambient vapour depletes the SWI composition of the water vapour. Furthermore, evaporation of droplets, similarly to ocean evaporation, tends to increase the d-excess in water vapour. Additionally, evaporatively cooled air beneath the cloud base leads to downdrafts that bring in depleted water vapour from higher altitudes down to the surface. If precipitation occurs, the SWI composition of near-surface water vapour is thus affected by these processes. Consequently, the measured and modelled SWI composition should agree better in cases where the model is able to capture observed precipitation events. To this end, a precipitation rate estimation from the micro rain radar measurements during ACE is compared to the total hourly precipitation of $COSMO_{iso}$. Figure 23 shows the micro rain radar data and the model precipitation interpolated along Leg 1 and Leg 2. In order to relate the precipitation to the SWI composition, δ^2H is added as well.

$COSMO_{iso}$ is able to capture most of the observed precipitation events, although timing and magnitude often differ between ACE and the model. This finding holds for both Leg 1 and Leg 2. Furthermore, observations of precipitation and short-time variability of SWIs are related by a drop in δ^2H, especially for strong events. Prominent examples can be identified on 23 December 2016, 26/27 December 2016, 06 January 2017, 20/21 January 2017 for Leg 1 and 23/24 January 2017, 19–21 February 2017 for Leg 2, respectively. Dütsch et al. (2016) identified a V-shaped

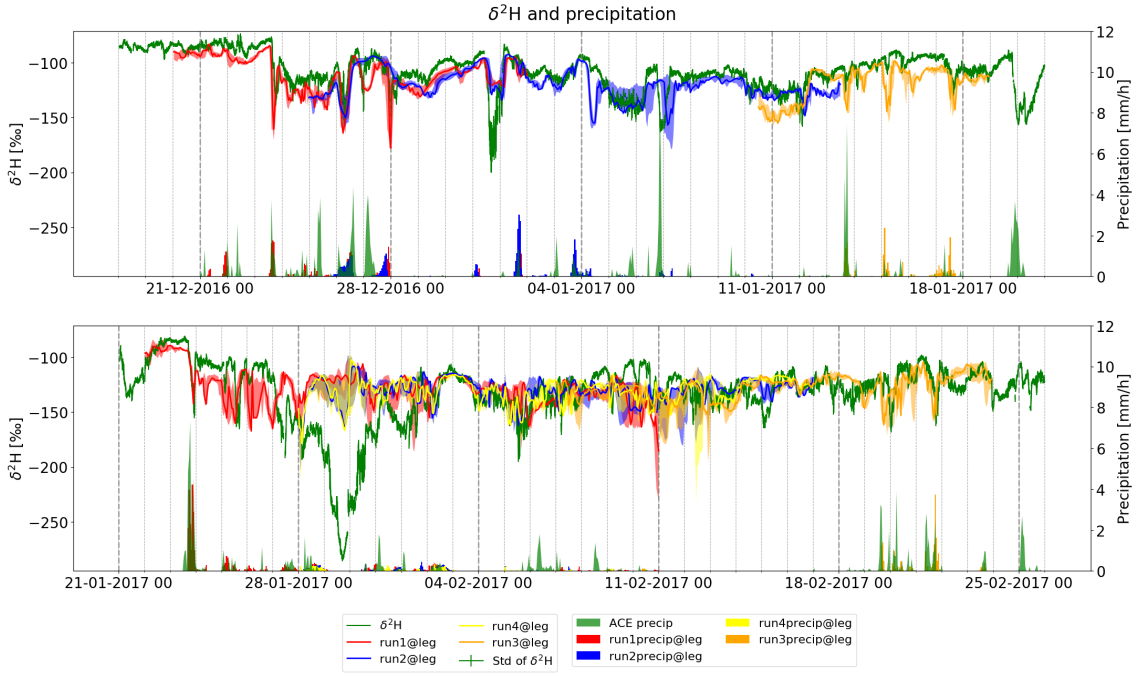

Fig. 23. Interpolation of precipitation along Leg 1 (upper panel) and Leg 2 (lower panel). The interpolation is shown for the three/four model runs (colored bars). For each model run, only the time period when the ACE position is within the model domain is considered. The shaded green area corresponds to the precipitation rate estimation from the micro rain radar.

evolution of δ^2H due to precipitation-vapour interaction, superimposed by a gradual depletion due to large-scale advection, during the passage of cold fronts as a typical pattern in both vapour and precipitation based on a model study. There are time periods where a good model performance in precipitation coincides with an increased performance in SWIs. The 23/24 January and the 19–21 February events serve as examples for such periods. The phase between 05–09 February, on the other hand, is an example where barely any precipitation is modelled in $\text{COSMO}_{\text{iso}}$, although substantial precipitation rates have been observed. Accordingly, this corresponds to a time period where SWI variability on short timescales is poorly represented in the model. Thus, it can be concluded that variability of model performance in precipitation and SWIs is, to some extent, related. There are, however, also events for which this finding does not hold: $\text{COSMO}_{\text{iso}}$ and observed precipitation agree well during 27/28 January, nevertheless the modelled and observed δ^2H values differ substantially.

The assessment of the influence of precipitation reveals that the model performance of $COSMO_{iso}$ with respect to precipitation and SWIs is, to some extent, related. Missing precipitation or biases with respect to timing and intensity in the model can lead to wrong SWI fluctuations on daily timescales. However, model shortcomings in precipitation can not serve as an exclusive explanation. In the context of this thesis, only the total amount of precipitation is considered. In future studies, it would be interesting to include a hydrometeor classification (rain, snow) in the analysis to further explore how cloud microphysical processes affect the model performance.

3.1.7 The influence of fractionation during snow sublimation

The extended model evaluation including both ECHAM5-wiso data (Subsection 3.1.3) and $COSMO_{iso}$ data along Leg 1 (Subsection 3.1.5) revealed that the observed model shortcomings are most likely related to non-fractionating snow- and ice-atmosphere interactions in $COSMO_{iso}$ and the simplified sea ice treatment altering air-sea interactions. Christner et al. (2017), using $COSMO_{iso}$ in the Arctic region, achieved a better agreement between their model results and observations by, amongst other adjustments, assuming equilibrium fractionation during surface snow sublimation or deposition over ice. Additionally, they increased the maximal snow albedo from 0.7 to 0.8, which led to an improved agreement with radiation measurements. Motivated by the findings of this thesis and the study of Christner et al. (2017), this chapter analyses an additional model run along Leg 2. The same model setup was used as for run 1 except for the incorporation of equilibrium fractionation during surface snow sublimation and deposition and an adjusted snow albedo, closely following Christner et al. (2017). The run is referred to as run 1_{snowfrac}.

Figure 24 shows the difference of averaged fields between the original run 1 and run 1_{snowfrac}. As expected, the adjusted setup does not lead to significant differences over the open ocean for any variable. Over the Antarctic continent, however, the averaged fields differ substantially. Equilibrium fractionation depletes the SWI composition of the near-surface vapour. This results in a decrease of up to $-20‰$ and $-160‰$ for $\delta^{18}O$ and $\delta^{2}H$, respectively. For the d-excess, two contrasting pattern emerge.

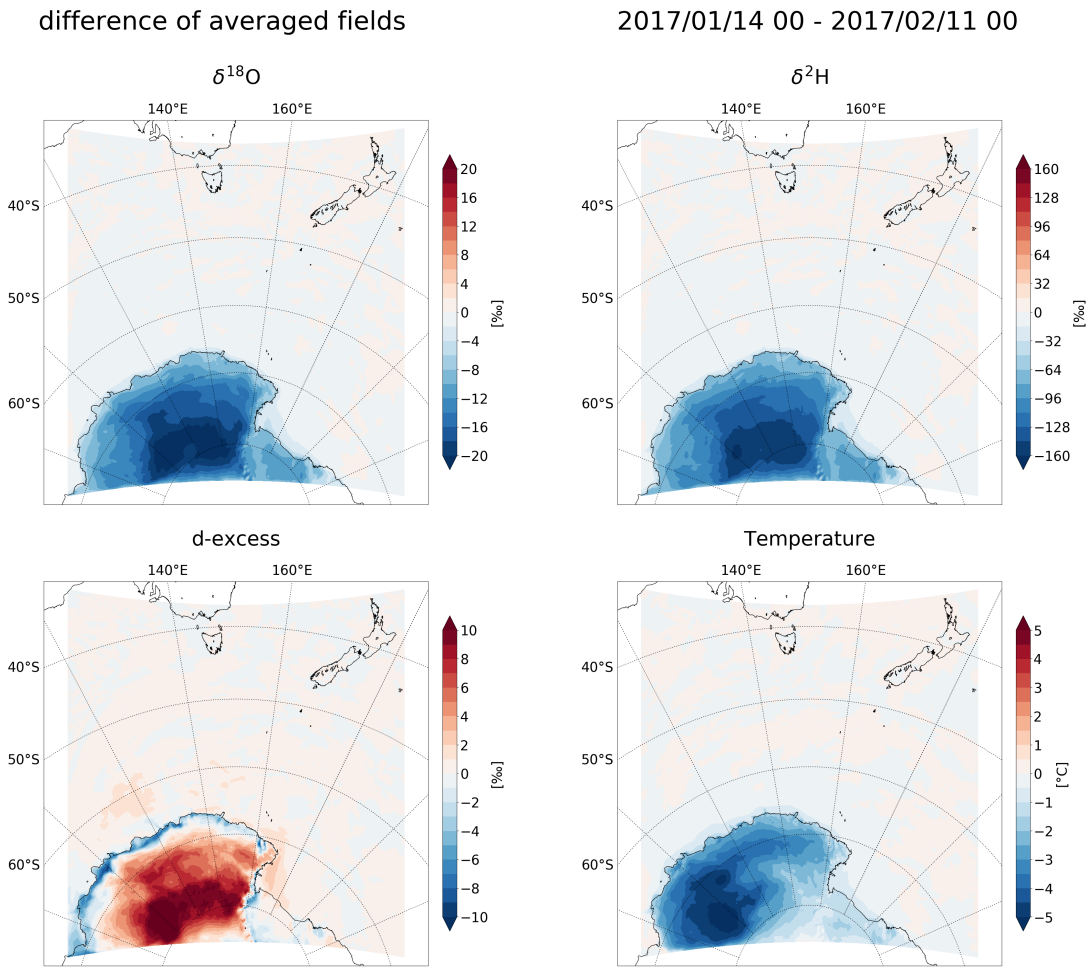

Fig. 24. Difference of averaged fields (δ^{18}O, δ^{2}H, d-excess, temperature) at each grid point at the lowest model level for run 1 and run 1_{snowfrac} (i.e. run 1_{snowfrac} − run 1).

In the interior of Antarctica, run 1_{snowfrac} shows an elevated d-excess (up to 10‰) compared to run 1. This finding is a result of the δ-scale effect described by Dütsch et al. (2017), which acts to increase d-excess values under equilibrium conditions in strongly depleted environments. In contrast to the interior, mean d-excess values are lower along the coast of Antarctica. Possibly, this pattern is related to fractionation during depositional fluxes (frost formation) in the run 1_{snowfrac}. Temperature, in turn, decreases substantially (up to -5 °C) as a result of the higher snow albedo. Since equilibrium fractionation is temperature dependent, this shift contributes to a stronger depletion of the SWI composition in water vapour over Antarctica.

The comparison of averaged fields revealed substantial differences between run 1 and run 1_{snowfrac}. In a next step, the model performance in SWIs between

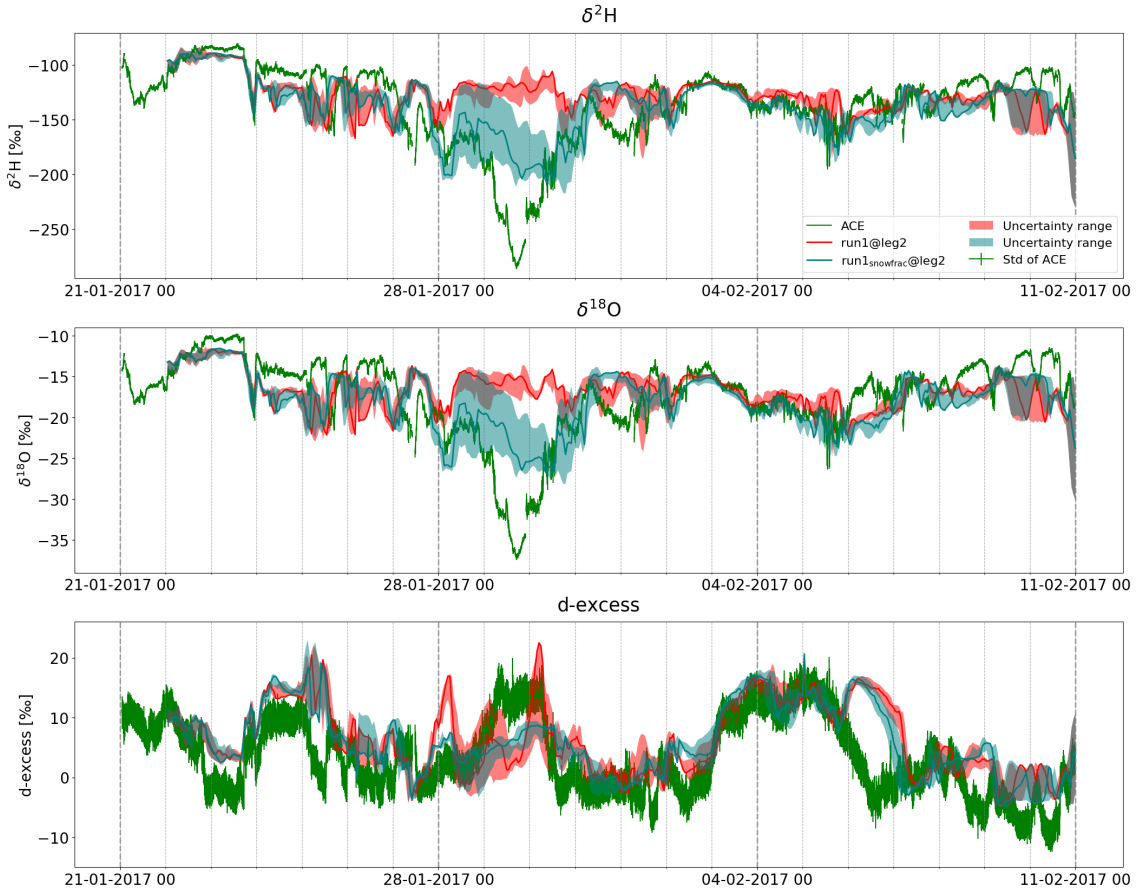

Fig. 25. Interpolation of isotope variables δ^2H, δ^{18}O and the d-excess from run 1 and run 1_{snowfrac} along the second ACE Leg.

the two runs is compared. Figure 25 shows $\text{COSMO}_{\text{iso}}$ data of run 1 and run 1_{snowfrac} interpolated along the ship track of Leg 2. During most of the time, the interpolations are similar. Regarding the Mertz event (end of January), however, large differences exist. While run 1 shows no isotopic depletion during the whole time of the event, δ-values decrease significantly for the run 1_{snowfrac}. The initial drop and the minimum are captured, although the decrease is delayed in the model and values are still too large in run 1_{snowfrac} compared to the observations. The last phase of the event, where the SWI composition increases again, is captured well.

Figure 26 compares model and observations in scatterplots. As observed in Fig. 25, the model error for the Mertz event is still present in the δ-variables, but decreases significantly. Furthermore, the temperature bias for the Mertz event decreases as well, which leads to a higher temporal correlation for temperature

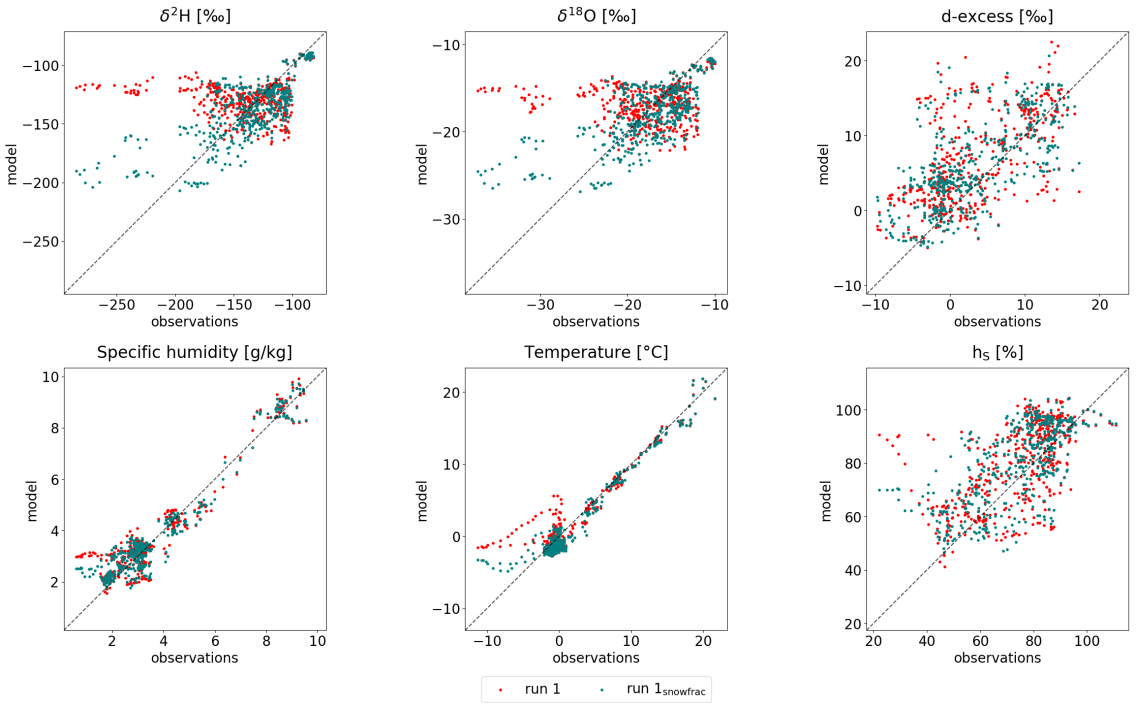

Fig. 26. Scatterplots of observations and interpolated model data for run 1 and run 1_{snowfrac}.

(0.97) compared to run 1 (0.94). The same finding holds for h_S (correlation of 0.68 for run 1_{snowfrac} compared to 0.60 for run 1) and, to a smaller extent, for specific humidity (correlation of 0.96 for run 1_{snowfrac} compared to 0.95 for run 1).

To complete the analysis, Fig. 27 compares the model performance in SWIs for run 1 and run 1_{snowfrac} in Taylor diagrams. The better representation of the Mertz event with the new setup leads to an improved skill for the δ-variables. The $RMSE$ decreases (13.3‰ for δ^2H and 1.7‰ for δ^{18}O). Concurrently, the correlations increase strongly (from 0.1 to 0.7 for both of the δ-variables) and modelled standard deviation differs less from the observed values. The statistical scores for d-excess show little change (correlation increases from 0.61 to 0.67).

From the comparison of the model performance, several conclusions can be drawn. First of all, the strong increase in the correlations reveals that the Mertz event effectively is the reason for the low correlation values of run 1. Secondly, the improved model performance in δ-variables, now aligning with the performance in the d-excess for run 1_{snowfrac}, points out that missing equilibrium fractionation during

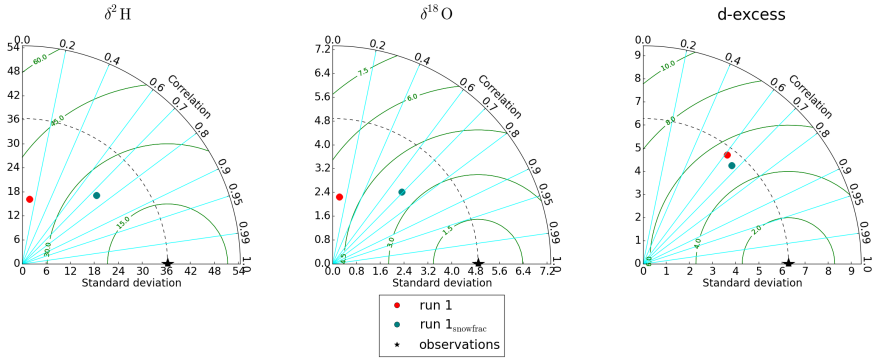

Fig. 27. Taylor diagrams for the isotopic variables δ^2H, δ^{18}O and the d-excess for run 1 and run 1_{snowfrac}.

snow-atmosphere interaction is a main reason for the observed model shortcomings. However, since fluctuations on short timescales are still only partly captured by $\text{COSMO}_{\text{iso}}$, other factors additionally affect the model performance. Possibly, non-equilibrium processes during snow- and ice-atmosphere interactions are important as well. Future studies are needed on snow-atmosphere interactions to include non-equilibrium isotopic fractionation into the parametrisation of snow-atmosphere surface fluxes of $\text{COSMO}_{\text{iso}}$. Furthermore, SWIs could be incorporated into the thermodynamic sea ice module of $\text{COSMO}_{\text{iso}}$. This might improve the representation of short-term fluctuations of SWIs and therefore consequently increase the skill at high latitudes.

3.2 Mertz event

The Mertz event corresponds to a period at the end of January, which lasted from approximately 28 January 00 UTC to 31 January 2017 00 UTC. During the event, exceptionally low δ-values were measured at the position of the ship at the Mertz glacier. Concurrently with the V-shaped evolution of $\delta^{18}O$ and $\delta^{2}H$, the d-excess increased, while temperature, specific humidity and h_S dropped (see in Fig. 10 and 9). Due to southerly winds measured during the Mertz stay, the air masses most likely originated from the interior of Antarctica, where low temperatures and distillation during meridional moisture transport lead to a strong isotopic depletion of the near-surface vapour (known as the temperature effect, e.g. Dansgaard, 1964). Antarctic air masses presumably have been transported towards the coast by a (katabatic) wind event during this time period. Since the Mertz event has not been captured by the original model setup, it will be analysed in detail in this section.

3.2.1 The effect of an increased horizontal resolution

Motivated by the poor performance of the original model runs 1 and 2 regarding the Mertz event, an additional model run has been performed with an increased horizontal resolution (see also Subsection 3.1.1). The surface elevation for run 2 at lower and higher resolution is illustrated in Fig. 28. The increased resolution leads to a more detailed representation of the topography along the Antarctic coastline, although differences are small in the region of the Mertz glacier. As seen in Fig. 10, the run at doubled horizontal resolution does not differ significantly from the original run 2. It can thus be concluded that, either, topography-induced effects are not the main reason for the poor model performance during the Mertz event, or, that for a more realistic representation of the steep Antarctic coastline, an even higher resolution might be necessary.

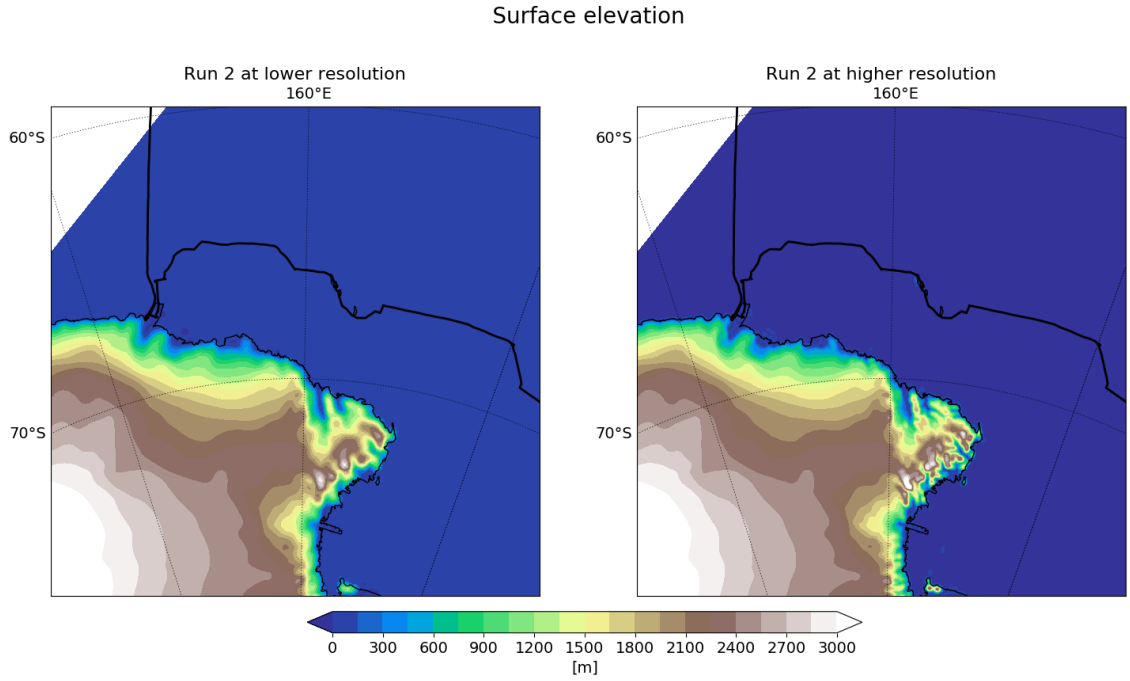

Fig. 28. Topography for run 2 with a horizontal resolution of 0.125° (left panel) and for run 4 with a horizontal resolution of 0.0625° (right panel).

3.2.2 Trajectory-based analysis of the influence of snow sublimation fractionation

This subsection contrasts the differing outcome for run 1 and run 1_{snowfrac} regarding the Mertz event from a Lagrangian point of view with the aid of backward trajectories (see Section 2.3 for the trajectory setup). Trajectories ending at pressures > 900 hPa are selected to be representative for the near-surface SWI composition measured at the ship's position.

The temporal evolution of the event can be split into three periods. The first part corresponds to the onset of the Mertz event (28 January 00 UTC until 28 January 12 UTC). It is represented by Fig. 29 showing backward trajectories ending at the ship's location at 28 January 06 UTC (colored by traced δ^2H). The comparison of run 1 (left panel) to run 1_{snowfrac} (right panel) reveals differences regarding the course of the trajectories. Although a part of the trajectories from run 1 originates from Antarctica, they merge in the western Ross Sea and follow the Antarctic coastline, bringing enriched air masses to the Mertz glacier. Trajectories from run

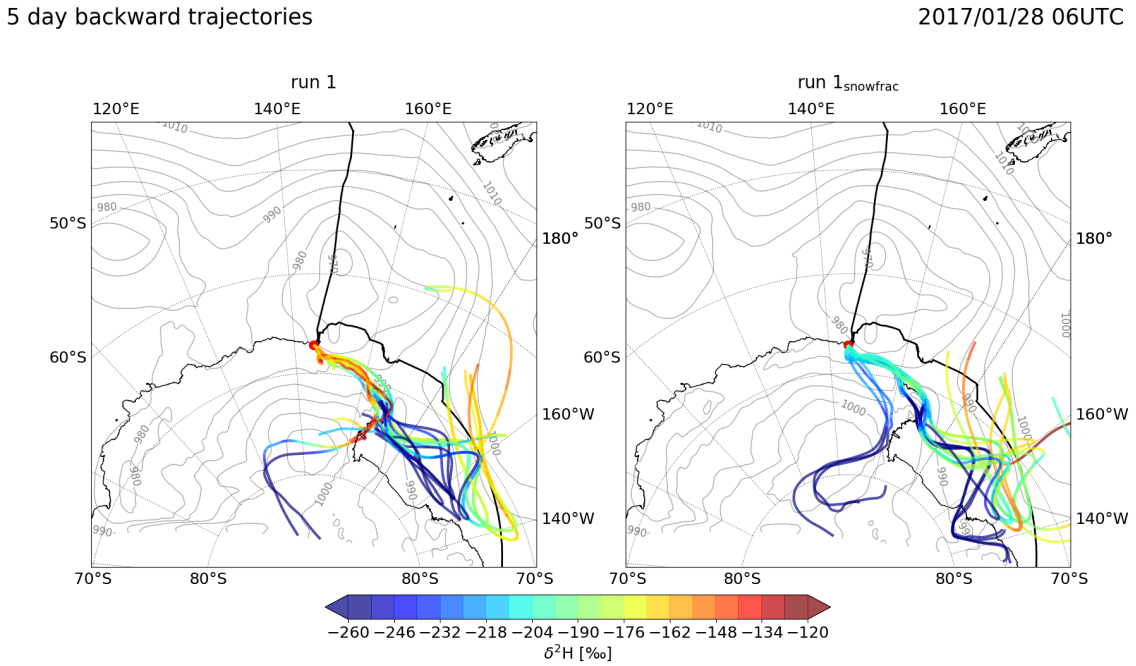

Fig. 29. Backward trajectories ending at the ship's position at 28 January 2017 06 UTC in a vertical column below 900 hPa for run 1 (left panel) and run 1_{snowfrac} (right panel). The last 5 days are shown and the trajectories are colored according to their δ^2H composition. Additionally, the sea level pressure at the end time of the trajectories is added.

1_{snowfrac}, on the other hand, can be split up into two distinct air streams. While the majority of the air parcels (corresponding to trajectories ending at higher levels) follow the coastline, the trajectories ending closest to the surface directly stem from the interior of the continent. As a consequence, they bring air masses with a more depleted isotopic composition to the position of the ship. Since the SWI extensions in $\text{COSMO}_{\text{iso}}$ are purely diagnostic, differences in the dynamics are caused by the adjusted albedo or numerically induced differences between run 1 and run 1_{snowfrac}. Apart from differing transport pathways, the trajectories following the coastline show a much lower δ^2H as well (decrease of more than 50‰ compared to run 1). This difference is a consequence of the equilibrium fractionation in run 1_{snowfrac}, leading to more depleted δ-values in the near-surface vapour in proximity to Antarctica (see also in Fig. 24). Due to the (partly) different origin of air masses, but also the additional fractionation process included into $\text{COSMO}_{\text{iso}}$, the model performance for run 1_{snowfrac} for the onset of the Mertz event is satisfying (see in Fig. 25).

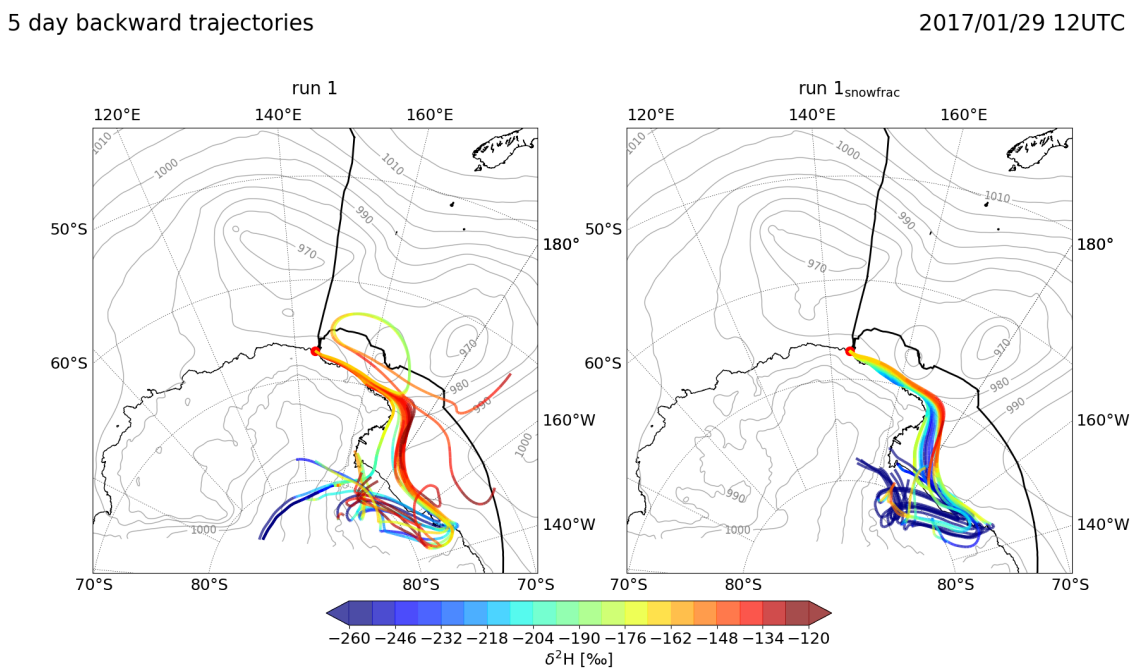

Fig. 30. The same as Fig. 29 but at 29 January 2017 12 UTC.

The second phase of the Mertz event, corresponding to the period where measured values dropped and reached a minimum, lasted from 28 January 18 UTC until 29 January 2017 18 UTC. During this time interval, the air mass origins differ little between run 1 and run 1_{snowfrac}. 29 January 2017 12 UTC has been chosen to represent this period in Fig. 30. The majority of the air parcels originate from Antarctica, pass over the Ross Sea afterwards and follow the coastline in the form of barrier winds towards the Mertz glacier. While δ^2H along the trajectories of run 1_{snowfrac} is significantly lower compared to run 1, there is still a large bias between $\text{COSMO}_{\text{iso}}$ and the measurements for that time period. Since the model error related to SWIs has been reduced in run 1_{snowfrac}, it can be speculated that the remaining discrepancy is caused by errors in the dynamics in $\text{COSMO}_{\text{iso}}$, simulating air masses following the coastline instead of originating from the interior of Antarctica.

During the last time period of the Mertz event, lasting from 30 January 2017 00 UTC until 31 January 2017 00 UTC, a substantial part of the trajectories proceed over the Antarctic ice shield before they arrive at the vessel's position, as illustrated in Fig. 31 for 30 January 2017 12 UTC. The pathways of air parcels in run 1 and run 1_{snowfrac} are similar to each other. With respect to the δ^2H transported along them, however, they vary strongly. The SWI composition along trajectories

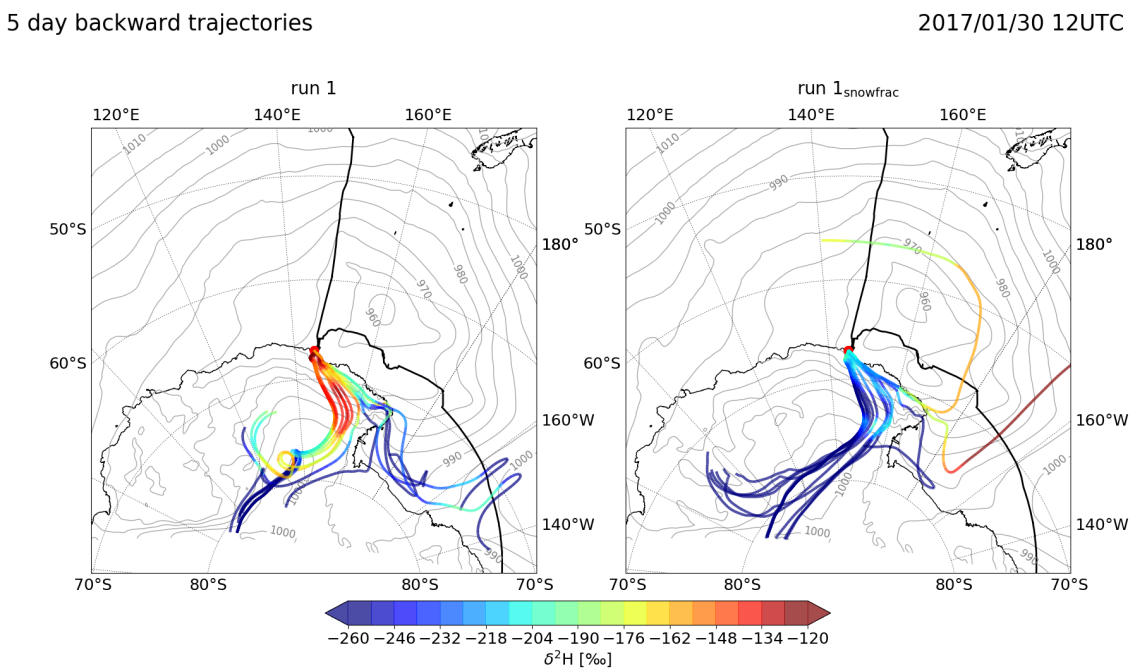

Fig. 31. The same as Fig. 29 but at 30 January 2017 12 UTC.

of run 1 gets enriched during the transport over the continent ($> -120‰$). In contrast, trajectories of run 1_{snowfrac} are associated with much lower δ^2H values ($< -260‰$) and show only a weak enrichment trend along the transport pathway. This outstanding difference has a strong impact on the model performance of $\text{COSMO}_{\text{iso}}$: While the interpolated SWI composition shows no decrease for run 1, it reaches a minimum for run 1_{snowfrac}. As a consequence, measured and modelled values of run 1_{snowfrac} agree well for this last phase of the Mertz event.

To summarize, this trajectory-based analysis of the Mertz event again confirmed the added value of implementing equilibrium fractionation during surface snow-atmosphere fluxes into $\text{COSMO}_{\text{iso}}$. The SWI composition along trajectories is consistently lower compared to run 1 during the event. If, additionally, air masses originate from the interior of Antarctica and do not come into contact with the ocean before arriving at the ship's position, $\text{COSMO}_{\text{iso}}$ agrees with the measurements. Furthermore, the different trajectory pathways in Fig. 29 reveal that small changes in the model dynamics, either induced by the change of the temperature field over Antarctica or by numerically induced differences between run 1 and run 1_{snowfrac}, can lead to substantial differences and thus affect the model performance.

3.3 Ross Sea event

This section focuses on the previously mentioned Ross Sea event (see for instance in Subsection 3.1.1), lasting from 03 February 2017 00 UTC until 06 February 2017 12 UTC. It is structured as follows: First, a short overview of the event is given with the aid of contour maps and vertical cross sections. In a second step, near-surface backward trajectories (ending at pressures > 960 hPa at 04 February 2017 12 UTC, see Section 2.3 for the trajectory setup) are used to characterise the air masses from a Lagrangian point of view. The last subsection applies the box model, as presented in Section 2.4, along the selected trajectories. The relative importance of ocean evaporation and MBL mixing for the SWI composition measured at the ship's position during the Ross Sea event is quantified. The entire analysis is based on model output from run 1_{snowfrac}.

3.3.1 Overview of the event

All overview figures are shown at 04 February 2017 00 UTC, corresponding to a time where the majority of the selected backward trajectories (ending 12 h later) are over the Ross Sea (see also Fig. 34). The Ross Sea event is categorised as a cold air outbreak (CAO). Marine CAOs can be described as an outflow of cool, continental air masses over the warmer ocean. The cyclone in the Eastern Ross Sea induces a northward flow, which advects Antarctic air masses towards the Ross Ice Shelf and over the Ross Sea (Fig. 32, left panel). Papritz et al. (2015) identified cyclone-induced CAOs as a frequently occurring phenomenon in the Ross Sea. The event is characterised by large air-sea temperature differences in the region where Antarctic air masses impinge on the ocean and at the outer edge due to strong cold-air advection (Fig. 32, right panel).

As the air masses of CAOs propagate over the ocean, they enhance turbulent heat fluxes from the sea into the atmosphere (Papritz et al., 2015). This typical characteristic of CAOs is observed for the Ross Sea event as well (Fig. 33). The event is characterised by both elevated sensible and latent heat fluxes of similar magnitude, though latent heat fluxes are slightly larger. The fluxes exhibit two maxima which coincide with the regions of largest air-sea temperature differences and air mass humidity deficits.

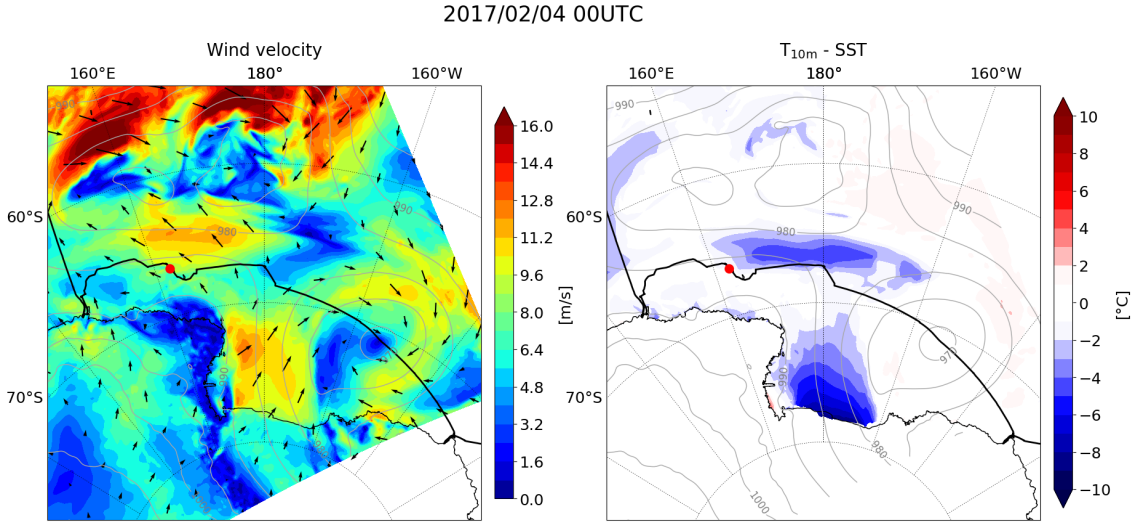

Fig. 32. Wind velocity at the lowest model level (colors) and wind vectors at 04 February 2017 00 UTC (left panel); difference between temperature at the lowest model level (virtually corresponding to 10 m above sea level) and the surface temperature over ocean at 04 February 2017 00 UTC (right panel). Additionally, the sea level pressure is indicated by grey contours and the ACE Leg including the vessel's position at 04 February 2017 00 UTC is displayed (black line, red dot).

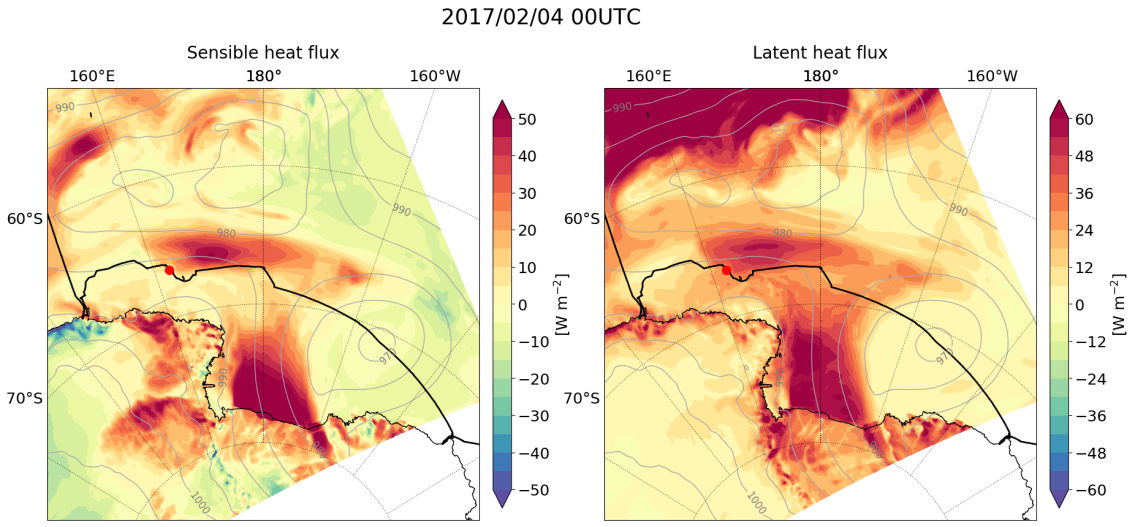

Fig. 33. Same as Fig. 32 but for sensible heat flux (left panel) and latent heat flux (right panel).

Since the cold Antarctic air masses are very dry, they are strongly undersaturated with respect to the warmer ocean surface, as illustrated in Fig. 34 (left panel). Air masses of the CAO are characterised by distinctively lower h_S. The substantial

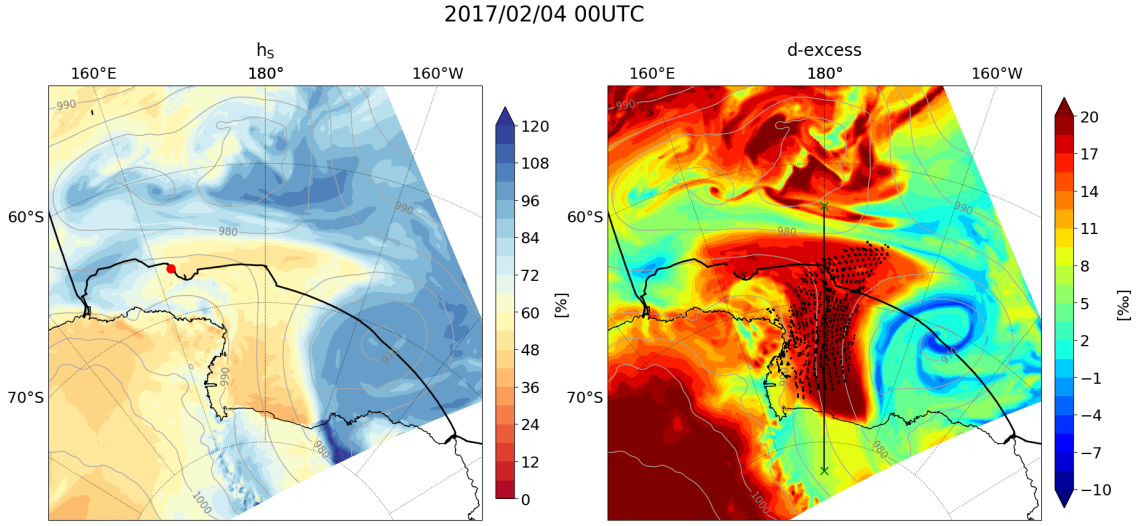

Fig. 34. Same as Fig. 32 but for h_S (left panel) and d-excess at the lowest model level (right panel). In the right panel, the course of the cross sections shown in Fig. 35 is added (black line, green crosses) and the position of the trajectories ending at 04 February 2017 12 UTC is indicated by black points.

undersaturation indicates conditions out of thermodynamic equilibrium, as it is typical for a ventilated environment during ocean evaporation. An elevated d-excess, as a measure for non-equilibrium effects during isotopic fractionation, confirms this finding (Fig. 34, right panel). The d-excess can therefore serve as an indicator of the evaporation conditions during the CAO.

In a next step, meridional cross sections of isotope variables and specific humidity are shown in order to characterise the vertical structure of the Ross Sea event (Fig. 35). The latitudinal extent of the cross sections is visible in Fig. 34. Since the focus of this section lies on boundary layer processes, the vertical axis is restricted to the lowest 2000 m. The cross sections reveal a strong contrast regarding the state of the boundary layer between the ice shelf and the ocean (separated by the black triangle). Over the ice, the boundary layer is confined to shallow levels (500 m) and stably stratified, the meridional temperature gradient is reversed. Shortly before the coastline is reached, conditions change: While temperature reaches a minimum and increases again with decreasing latitude, the stratification of the boundary layer becomes approximately neutral. The potential temperature contours even indicate unstable conditions in the lowest 100 m ($\frac{\partial \Theta}{\partial z} < 0$). At the same time, the boundary layer expands and reaches a height of 1400 m. Con-

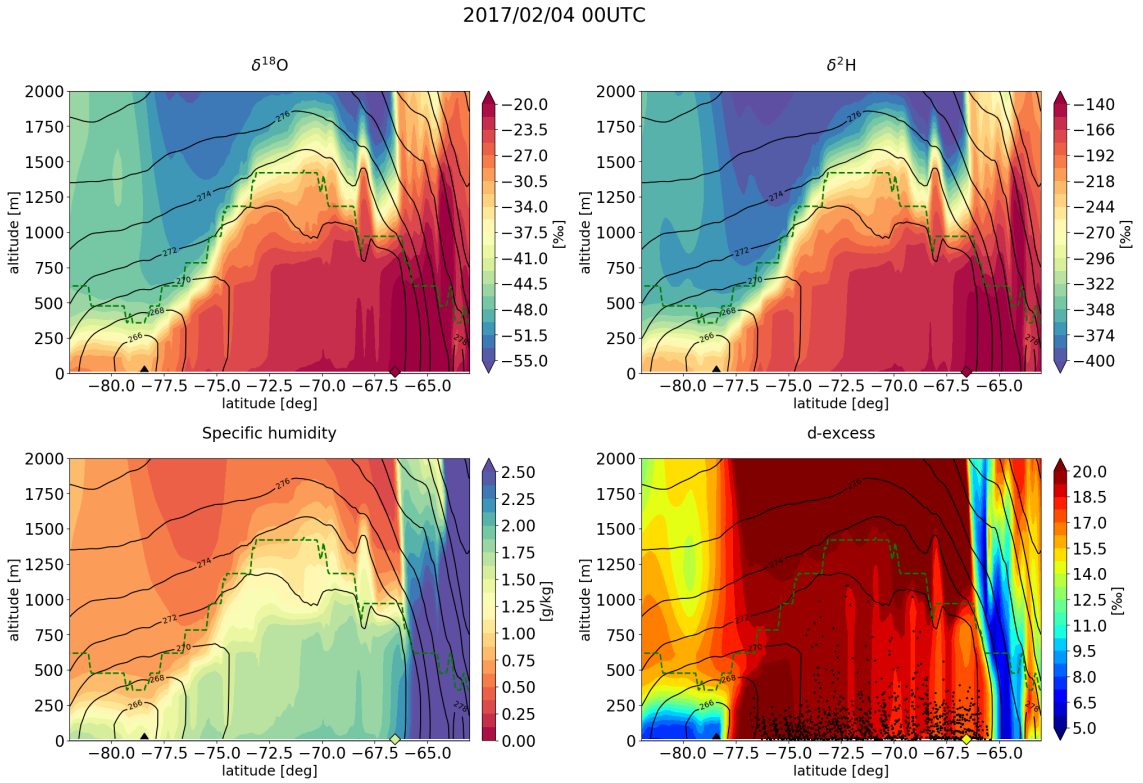

Fig. 35. Meridional vertical cross sections for $\delta^{18}O$ (upper left panel), $\delta^{2}H$ (upper right panel), d-excess (lower right panel) and specific humidity (lower left panel). Potential temperature contours (black lines) and the boundary layer height (green dashed line) are added. Additionally, the latitude of the coastline (black triangle) and the ACE position at 04 February 2017 00 UTC (diamond) are shown. The ACE markers are colored according to the measured value at this time ($\delta^{18}O = -19.8‰$, $\delta^{2}H = -143.7‰$, d-excess = 14.5‰, specific humidity = 1.6 g/kg). In the d-excess cross section, the positions (latitude, altitude) of the selected trajectories are displayed.

ditions over sea are thus favourable for intense mixing on the scale of the entire MBL.

Turbulent vertical exchange leads to a rather uniform vertical distribution of the isotopic variables and the specific humidity over the Ross Sea, in contrast to the conditions over the ice shelf, where a gradient within the boundary layer is present. Besides this, the boundary layer top marks the strong transition to free-tropospheric air, which is characterised by a much more depleted isotopic composition, a higher d-excess (over the ocean) and low specific humidity. For the land-sea contrast, the δ-variables show an enrichment trend with decreasing latitude, while humidity increases. A striking feature is the very strong gradient in the d-excess at the ice-ocean margin. This is consistent with the spatial pattern presented in Fig. 34.

The outer margin of the Ross Sea event (at 66 °S) is associated with a strong baroclinic zone, as it is typical for marine CAOs (Papritz et al., 2015). Air mass characteristics again change drastically (isotopic enrichment, d-excess decrease, humidity increase) where the cold polar air masses impinge on mid-latitude air of the SO storm track. The low d-excess values are probably caused the combined influence of ice cloud microphysical processes, strong downdrafts and below-cloud fractionation processes.

3.3.2 Lagrangian characteristics of air masses

After the Eulerian perspective on a particular instant of the Ross Sea event, this subsection complements the event characterisation by considering the Lagrangian point of view. To this end, Fig. 36 shows the temporal evolution of temperature, potential temperature, specific humidity and evaporation along the trajectories. The time axis is normalised with respect to the moment when the trajectories pass over the land-sea boundary.

The Antarctic coastline marks the zone where the characteristics of the air masses start to change drastically. As the cold, continental air passes over the ocean, both temperature ($\Delta \mathrm{T} = 7K$) and potential temperature ($\Delta\Theta = 6K$) increase substantially. The coherent change of both of them is largest in the first half after the land-sea boundary and indicates that temperature increases due to sensible heat fluxes from the ocean into the atmosphere (see also Fig. 33). In contrast to that, temperature shows no trend as long as the trajectories are over Antarctica, while potential temperature slightly decreases. Possibly, this is a consequence of radiative cooling approximately compensating adiabatic warming during the slight descent of the trajectories before they reach the Ross Sea. Specific humidity, in turn, doubles from 1 g/kg over the Ross Ice Shelf to 2 g/kg. This is in accordance with the sharp increase of evaporation from values only slightly above 0 kg/m^2 to 0.08 kg/m^2. The temporal evolution of evaporation along the trajectories, with the initially strong increase and a slow decrease afterwards, again agrees with the spatial pattern visible in Fig. 33. Overall, according to its spatial features (strong ocean-atmosphere temperature contrast, enhanced turbulent fluxes, reduced MBL stability, baroclinic zone) and the Lagrangian characteristics of the air masses, the Ross Sea event can thus be categorized as a typical example of a marine CAO in the Ross Sea (Papritz

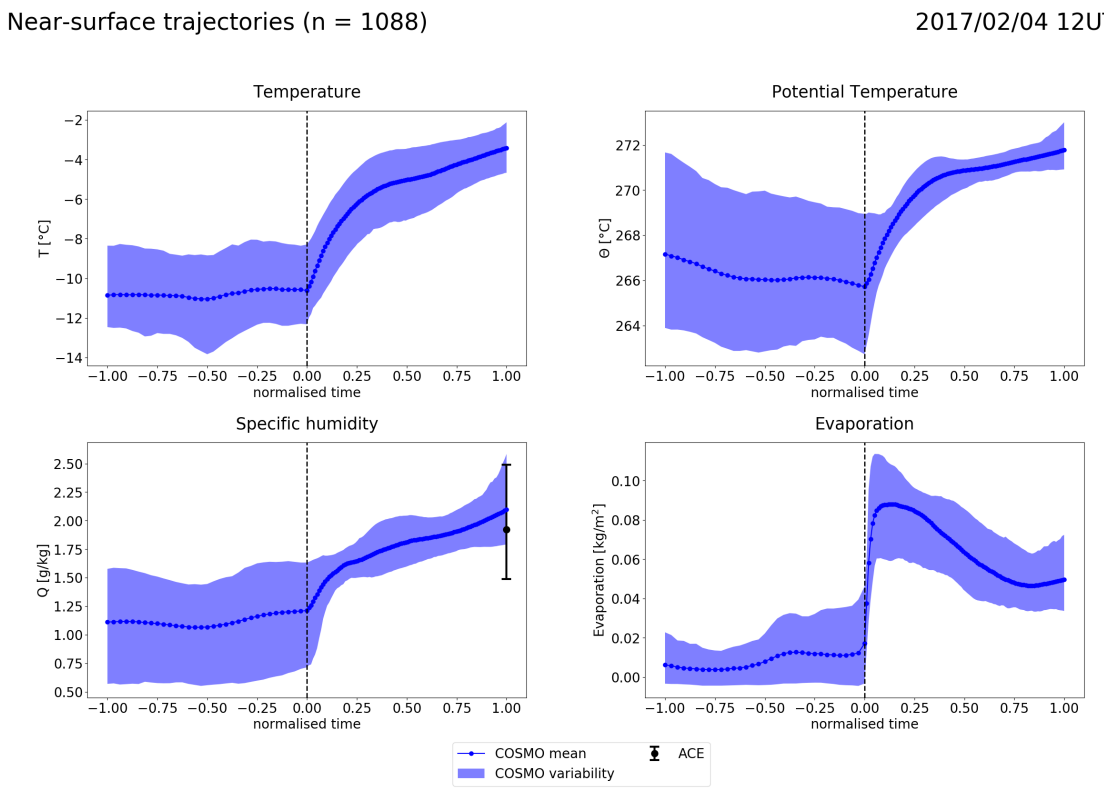

Fig. 36. Mean (dotted lines) and variability (shaded areas; from 10th to 90th percentile) along the selected trajectories for temperature (upper left panel), potential temperature (upper right panel), specific humidity (lower left panel) and evaporation (lower right panel). The time axis is normalised by linear temporal interpolation of the time periods between the moment when the air parcels pass the land-sea boundary and arrive at their ending location and selecting the last 33 h (corresponding to the mean time period over sea) before they come over the ocean as the analogue over the continent. For specific humidity, ACE observations are added (black dot: 04 February 12 UTC; black bar: range confined by minimal and maximal observed values between 04 February 00 UTC and 05 February 18 UTC).

et al., 2015). In Subsection 3.3.3, the focus will be on the SWI signal of the event.

3.3.3 Sensitivity studies with a trajectory-based box model

The Ross Sea event, as already seen in Fig. 10 and 34, is associated with an elevated d-excess, as it is typical for an event of strong ocean evaporation (Aemisegger and Sjolte, 2018). This subsection investigates the distinctive SWI signal of the event in order to attribute the different processes influencing the measured signal during ACE. To this end, the output of the $\text{COSMO}_{\text{iso}}$ model (run 1_{snowfrac}) is

compared to the box model simulations (for the box model setup see Section 2.4). The sensitivity of the SWI signal to entrainment of depleted, free-tropospheric air is studied in order to determine the influence of evaporation and mixing for the SWI signal. Furthermore, the Lagrangian box model framework is used to quantify the contribution of the different moisture sources (advection from Antarctica, ocean evaporation, entrainment of free-tropospheric humidity) to the humidity increase along the transport pathway.

In analogy to Fig. 36, Fig. 37 shows the SWI variables (δ^{18}O, δ^{2}H, d-excess) along the selected COSMO$_{\text{iso}}$ trajectories. Again, the land-sea boundary separates two distinct patterns. Antarctic air, before passing the coastline, is very depleted with respect to SWIs (δ^2H $= -260$‰, δ^{18}O $= -35$‰) and has a lower d-excess (10‰). Furthermore, the variability among the trajectories (indicated by the blue shaded area) is very large. As the air masses are transported over the Ross Sea, ocean evaporation leads to an enriching trend in the δ-variables (up to -150‰ for δ^{2}H and -20‰ for δ^{18}O) and a significant increase in the d-excess (up to 17‰), indicating non-equilibrium conditions during evaporation. In contrast to the time before reaching the coastline, the variability is lower. This points out that the trajectory population shares a common physical history during the transport over the ocean.

Changing the focus towards the box model simulations, Fig. 37 reveals that the simulation assuming evaporation to be the only process affecting the SWI signal (black line) is able to capture the observed trends, but shows a significant offset compared to the mean COSMO$_{\text{iso}}$ trajectory values. While the δ-variables are too enriched, the d-excess increase is underestimated. This indicates that at least one additional process besides ocean evaporation is influencing the SWI signal along the transport pathway. Since the near-surface trajectories unlikely experience substantial condensational processes (see the continuous moisture increase in Fig. 36) and upon considering the low-stability conditions in the MBL during the Ross Sea event (see Fig. 35), mixing of MBL air with depleted, free-tropospheric air can be identified as the potentially important process. Entrainment of dry and depleted, free-tropospheric air into the MBL partly compensates the enrichment trend caused by ocean evaporation. Since this air is associated with a very high d-excess (30‰ for

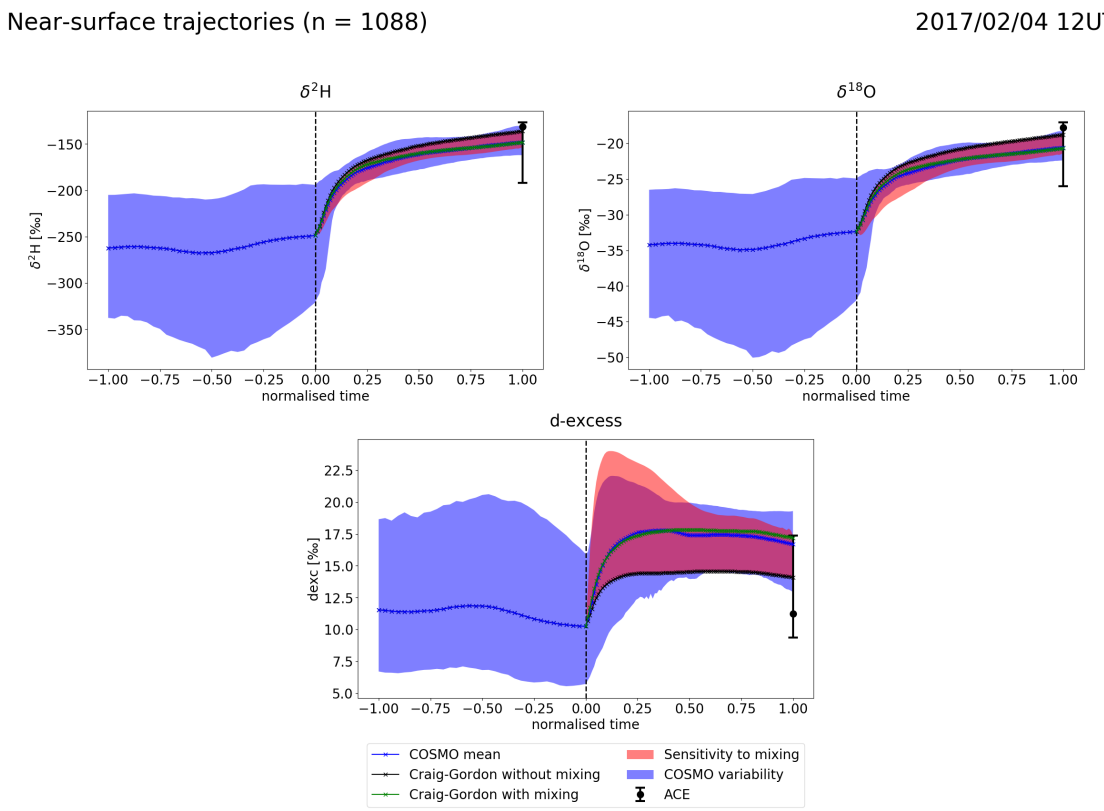

Fig. 37. Blue colors (lines and shaded areas) correspond to $\text{COSMO}_{\text{iso}}$ data traced along the trajectories, similar to Fig. 36 but for the SWI variables δ^2H, δ^{18}O and the d-excess. The black line is the mean along the trajectories resulting from the box model if evaporation is assumed to be the only process affecting the SWI composition (no mixing). The red, shaded area corresponds to the range of the means of repeated simulations with the box model incorporating varying mixing contributions ($0 \leq f_1 \leq 0.5$) in order to represent the sensitivity of the box model to entrainment of depleted air masses. The green line depicts a box model simulation with $f_1 = 0.06$ and serves as an example which agrees well with the $\text{COSMO}_{\text{iso}}$ simulation. Additionally, ACE observations are added (black dot: 04 February 12 UTC; black bar: range confined by minimal and maximal observed values between 04 February 00 UTC and 05 February 18 UTC).

the chosen SWI composition of the depleted air, see also in cross section in Fig. 35), it is an important factor contributing to further increase the d-excess. The mixing sensitivity experiment (see red shaded area) shows that the modelled SWI signal is more sensitive to the mixing fraction (f_1) shortly after the land-sea boundary. During this initial phase of the event, the amount of humidity originating from ocean evaporation is still small. Therefore, the constant entrainment fraction has a larger impact than at a later stage. When trajectories arrive at their end position, the sensitivity range is more confined and smaller than the observed variability

along the $COSMO_{iso}$ trajectories (blue shaded area). The green curve corresponds to the mean of all trajectories for a particular box model setup with $f_1 = 0.06$. For this entrainment fraction, the box model agrees well with the $COSMO_{iso}$ trend. It can thus be said that, for the Ross Sea event, fresh ocean evaporate (with a fraction of 94%) and entrainment of depleted, free-tropospheric air (with a fraction of 6%) along the transport pathway govern the SWI signal simulated by $COSMO_{iso}$. Furthermore, the sensitivity assessment reveals a non-linear relation between the strength of the mixing and its impact. Initially, mixing with only a small fraction (compare black line and green line) leads to large differences in the outcome. As the fraction increases further, the sensitivity of the result gets progressively smaller (compare green line and the maximum of the red shaded area). This points out that MBL entrainment is a significant factor determining the near-surface SWI composition, even when only a small amount of free-tropospheric air is mixed downward.

Besides $COSMO_{iso}$ data and box model simulations, Fig. 37 and 36 show ACE observations at the ending time of the trajectories and the associated variability range from 04 February 00 UTC until 05 February 18 UTC, corresponding to the peak time of the CAO. ACE measurements of SWIs at 04 February 12 UTC deviate considerably from the mean along $COSMO_{iso}$ trajectories as well as the mean of box model simulations (more enriched δ-values, lower d-excess in the measurements). This is a consequence of the ship's position at the edge of the CAO during this time, compared to the trajectory arrival points situated in the center of the CAO air mass (see also Fig. 7). The variability ranges of measured values during the Ross Sea event, however, include the end values of $COSMO_{iso}$ and the box model simulation for $f_1 = 0.06$. Possibly, this indicates a variable importance of MBL mixing for air masses measured at the ship's position during the event. Observations along the enrichment path of the CAO air mass constitute an important constraint to validate the budget model approach besides $COSMO_{iso}$ data along the trajectories. However, the trajectory ending points for the Ross Sea case were chosen to best match the position of the front edge of the CAO air mass, instead of following the position of the vessel during the time period. Furthermore, the ship track proceeds close to the edge of the CAO. Due to this discrepancy, the verification of the box model with ACE observations is not trivial. Future studies could address this by adjusting the trajectory setup or the time instant considered in order to minimize the discrepancy.

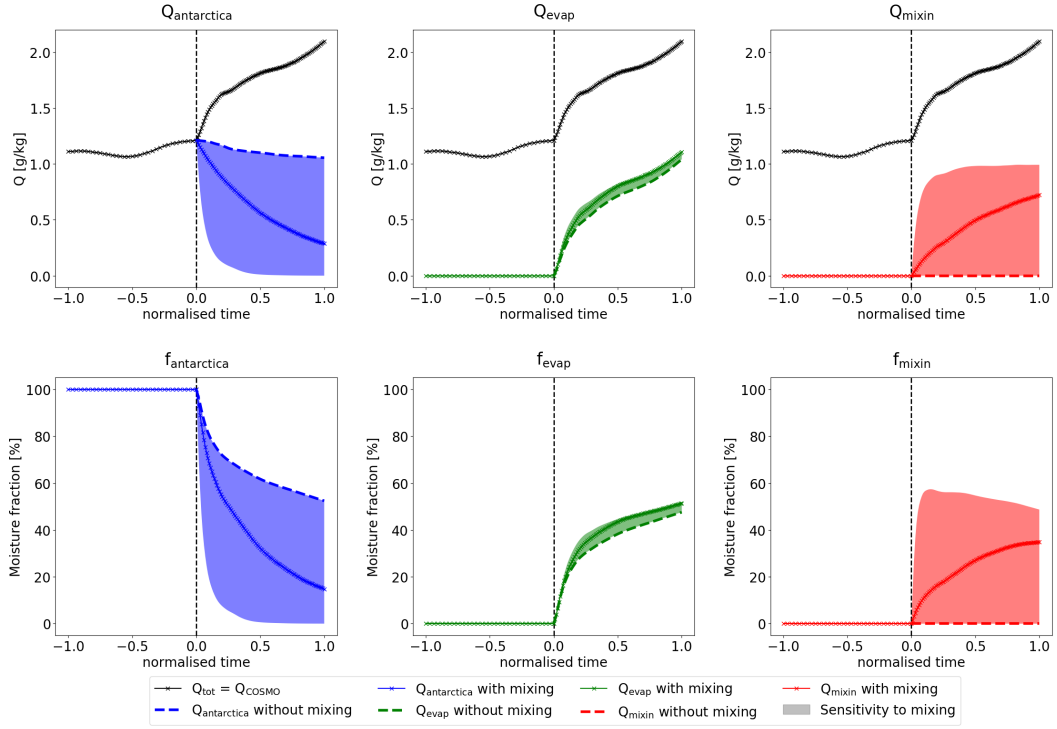

Fig. 38. Lagrangian humidity budget along the selected trajectories. The time axis is normalised like in Fig. 36 and 37. The upper panel shows the absolute amounts of $Q_{antarctica}$ (left), Q_{evap} (center) and Q_{mixin} (right), the lower panel displays their relative fraction of the total humidity (in the same order). The black line represents the sum of all humidities and is equal to the specific humidity in Fig. 36. The dashed lines show the box model mean if no mixing is assumed ($f_1 = 0$), while the colored, crossed lines correspond to the box model simulation with $f_1 = 0.06$. The shaded areas, in turn, represent the sensitivity to mixing ($0 \leq f_1 \leq 0.5$).

Additionally to the SWI budget along the trajectories, a humidity budget has been implemented into the box model (see Section 2.4). Figure 38 shows results of the budget calculations for the three humidity categories ($Q_{antarctica}$, Q_{evap}, Q_{mixin}). In the case of no mixing ($f_1 = 0$), $Q_{mixin} = 0$ and the total humidity is separated into contributions from Antarctica and from ocean evaporation. As can be seen in Fig. 38, the absolute amount originating from Antarctica stays almost constant. The only possibility acting to lower $Q_{antarctica}$ in the no-mixing simulation is if $\Delta Q < 0$. For such cases, corresponding to episodic rainout events, the different humidities are assumed to decrease with a scaling according to their fraction of the total humidity at the respective time step (e.g. $\Delta Q_{antarctica,i} = \Delta Q_i \cdot \frac{Q_{antarctica,i}}{Q_{tot,i}}$). The small decrease

of Antarctic humidity, however, reveals that such cases rarely happen. The humidity from ocean evaporation, on the other hand, continuously increases, which acts to decrease $f_{antarctica}$ along the transport pathway. In the end, the total humidity doubles, with approximately equal contributions from Antarctica and ocean evaporation. If mixing is included into the box model, an additional category (Q_{mixin}) has to be considered for the humidity budget. The fraction from ocean evaporation is insensitive to the integration of mixing, in terms of total and relative amounts. Both of them (Q_{evap}, f_{evap}) slightly increase for an increasing mixing intensity. This indicates that the upward mixing of freshly evaporated humidity is compensated by a larger ΔQ_{evap} in the box model. The other two categories, however, show a strong sensitivity to entrainment. Antarctic humidity decreases faster due to outward mixing along the trajectories (down to 0.3 g/kg for $f_1 = 0.06$). Concurrently, downward mixing acts to increase the fraction of the free-tropospheric humidity (up to 0.7 g/kg for $f_1 = 0.06$). The highlighted box model simulation again shows that the outcome is initially very sensitive to small changes in the mixing intensity, while the sensitivity subsequently decreases for an increasing f_1. For this simulation, the contribution of ocean evaporation is similar to the simulation without mixing (50%). The fraction of Antarctic humidity, however, is much smaller (15%) whereas free-tropospheric humidity constitutes a significant part (35%) of the total humidity.

The newly developed box model confirms that entrainment of depleted air masses from the lower troposphere into the MBL significantly affects the near surface SWI signal in the case of a marine CAO. With the Lagrangian framework, including horizontal advection, ocean evaporation and MBL mixing, box model simulations with an entrainment fraction of 6% ($f_1 = 0.06$) are found to agree well with the $\text{COSMO}_{\text{iso}}$ model. This partly agrees with a recent study of Benetti et al. (2015), where they found near-surface δ-variables to be influenced by MBL entrainment. Their mixing model, however, suggested a small impact of mixing for the d-excess, which stands in contrast to the results from this thesis. Furthermore, the humidity budget calculations reveal that the influence of the initial humidity from Antarctica decreases fast, being replaced with downward mixed humidity from the free troposphere. Certainly, the box model framework presented in this study requires further development. Rayleigh distillation for cases where $\Delta Q < 0$ has to be included. Furthermore, the free-tropospheric composition could be taken out of

the $COSMO_{iso}$ model directly, instead of keeping it constant. Future studies could assess the sensitivity with respect to the initial SWI composition from Antarctica. In the context of this thesis, the MBL mixing process is assumed to be constant over time. However, turbulent transport by eddies rather exhibits an episodic character. It would thus be interesting to consider mixing as a temporally variable process along the trajectories in the future. Observations provide an important additional constraint for the budget model. The verification using point-measurements in a region with strong SWI gradients is, however, challenging and has to be further assessed in future studies.

Chapter 4

Conclusions and outlook

This thesis combines the isotope-enabled, regional numerical model $COSMO_{iso}$ with meteorological and laser spectrometer SWI measurements at a high temporal resolution, conducted during the ACE expedition circumnavigating Antarctica in the austral summer 2016/2017. Our goal was to, for the first time, evaluate the model performance of $COSMO_{iso}$ in the Southern Hemisphere and give a three-dimensional context to the measurements. Furthermore, the joint use of model simulations and observations has helped us to examine the different processes affecting SWI variability associated with a marine CAO.

Meteorological variables are found to be represented well near the surface along the ship track of Leg 1 and Leg 2. SWI variability is reliably reproduced under the offshore conditions along Leg 1, where ocean evaporation and the passage of mid-latitude weather systems constitute the driving force shaping the observed SWI signal. Along Leg 2, in proximity to Antarctica, the model performance is reduced compared to Leg 1. By contrasting simulations along Leg 2 and Leg 1, considering ECHAM5-wiso (the GCM providing initial and boundary fields) model data and assessing the sensitivity of run 1 along Leg 2 to the inclusion of equilibrium fractionation during surface snow sublimation and deposition, non-fractionating snow-atmosphere interactions are identified as one of the main reasons for the observed model shortcomings. This is particularly reflected in a superior representation of the pronounced drop in the δ-variables during the Mertz event (end of January), leading to much better overall skill of run $1_{snowfrac}$ (correlation for δ-variables increases from 0.1 to 0.7). A trajectory-based event

analysis confirms the added value of including equilibrium fractionation during snow-atmosphere interactions into $COSMO_{iso}$ and reveals that the model agrees well with observations whenever isotopic depletion over Antarctica and transport pathways from the interior of the continent towards the coast are both captured. Furthermore, the reduced temperature bias during the event indicates that the increased maximal surface albedo better captures Antarctic near-surface temperature conditions.

Nevertheless, fluctuations on short timescales are still not represented to the same extent in run $1_{snowfrac}$ as in the runs along Leg 1. It has thus to be emphasized that equilibrium fractionation during surface snow-atmosphere interactions can not be the only factor limiting the $COSMO_{iso}$ model performance in proximity to Antarctica. Including the non-equilibrium component of surface snow-atmosphere interactions into the model in the future may help to assess the importance of non-equilibrium fractionation effects for the observed SWI signal. Besides this, the simplified sea ice treatment used for the $COSMO_{iso}$ runs is, presumably, another reason for the observed model shortcomings. Currently, the model determines the presence of sea ice based on a surface temperature threshold condition, whereupon turbulent fluxes are strongly reduced in sea ice covered grid cells. Future studies could include SWIs into the prognostic sea ice module of $COSMO_{iso}$ in order to investigate the added value of a more sophisticated sea ice treatment and fractionating humidity fluxes between the (snow-covered) sea ice and the atmosphere. Another influencing factor, which has been addressed in the context of this thesis, is the dependence of the SWI signal on the modelled precipitation timing and intensity. However, future efforts are necessary in order to further investigate if the inability of $COSMO_{iso}$ to capture precipitation events (especially snow fall events) and the related fractionating processes is a major reason for the decreased model performance near the Antarctic continent. Furthermore, the model validation showed a systematic bias of modelled d-excess values towards higher values. The sensitivity assessment with run 1_{MJCW} indicated that an adjustment of the non-equilibrium fractionation factor could yield better d-excess model results for the SO region.

While the primary focus of this thesis has been on validating the $COSMO_{iso}$

model, the simulations revealed interesting isotopic features in the SO storm track region. Among them are pronounced gradients in the SWI composition along warm fronts associated with extratropical cyclones. Future studies could investigate these patterns in order to identify the underlying processes. Especially, it would be interesting to contrast the cross warm-frontal evolution of SWIs to the established V-shaped trend, superimposed to a gradual depletion, during the passage of cold frontal systems.

Additionally, a newly developed Lagrangian box model framework is presented. The budget model incorporates the processes of horizontal advection, ocean evaporation and MBL mixing, thereby iteratively solving equations for the SWI composition and the moisture budget. In a first case study, presented in this thesis, it is applied along backward trajectories calculated during a marine CAO into the Ross Sea. The budget model reveals that the exclusive consideration of ocean evaporation as the process determining the SWI signal (no mixing) leads to too enriched δ-values and a too low d-excess compared to the traced SWI trend. If, however, the evaporate (94%) is mixed with a depleted air mass from the free troposphere (6%) at each time step, the box model is found to agree well with the $\text{COSMO}_{\text{iso}}$ SWI composition along the trajectories. Under no-mixing conditions, the initial humidity from Antarctica stays almost constant over the ocean, such that in the end, ocean evaporation and Antarctic humidity equally contribute to the total moisture budget. If, however, entrainment of free-tropospheric air is included, downward mixing efficiently replaces the initial Antarctic contribution and a part of the ocean evaporate. The preliminary version of the budget model offers possibilities for further development. Fractionation during condensational processes can be incorporated via Rayleigh distillation. Up to now, mixing is considered as a constant process along the trajectories. Future studies could adapt the box model to explicitly include the temporal dependence of MBL entrainment. ACE observations offer an observational-based verification for the box model. An adjustment of the box model setup might facilitate the use of this additional constraint. Considering this, the methodology represents a promising approach in order to constrain the MBL moisture budget and MBL mixing with SWIs.

The validation of $\text{COSMO}_{\text{iso}}$ near Antarctica revealed the potential for further model

development in order to include all processes affecting SWI variability in water vapour at high latitudes. This is particularly meaningful considering the possibility to use SWIs as proxies for processes of the atmospheric water cycle and its dynamical drivers. The combined use of $\mathrm{COSMO_{iso}}$, the Lagrangian box model and measurements in an exploratory case study with the goal to constrain MBL mixing with SWIs constitutes an example for such an application.

Bibliography

Aemisegger, F., Pfahl, S., Sodemann, H., Lehner, I., Seneviratne, S. I., and Wernli, H. (2014). Deuterium excess as a proxy for continental moisture recycling and plant transpiration. *Atmos. Chem. Phys.*, 14(8):4029–4054.

Aemisegger, F. and Sjolte, J. (2018). A climatology of strong large-scale ocean evaporation events. Part II: Relevance for the deuterium excess signature of the evaporation flux. *J. Climate*, 31(18):7313–7336.

Aemisegger, F., Spiegel, J., Pfahl, S., Sodemann, H., Eugster, W., and Wernli, H. (2015). Isotope meteorology of cold front passages: A case study combining observations and modeling. *Geophys. Res. Lett.*, 42(13):5652–5660.

Aemisegger, F., Sturm, P., Graf, P., Sodemann, H., Pfahl, S., Knohl, A., and Wernli, H. (2012). Measuring variations of δ^{18}O and δ^{2}H in atmospheric water vapour using two commercial laser-based spectrometers: An instrument characterisation study. *Atmos. Meas. Tech.*, 5(7):1491–1511.

Benetti, M., Aloisi, G., Reverdin, G., Risi, C., and Sèze, G. (2015). Importance of boundary layer mixing for the isotopic composition of surface vapor over the subtropical North Atlantic Ocean. *J. Geophys. Res.: Atmos.*, 120(6):2190–2209.

Benetti, M., Lacour, J.-L., Sveinbjörnsdóttir, A., Aloisi, G., Reverdin, G., Risi, C., Peters, A., and Steen-Larsen, H. (2018). A framework to study mixing processes in the marine boundary layer using water vapor isotope measurements. *Geophys. Res. Lett.*, 45(5):2524–2532.

Butzin, M., Werner, M., Masson-Delmotte, V., Risi, C., Frankenberg, C., Gribanov, K., Jouzel, J., and Zakharov, V. I. (2014). Variations of oxygen-18 in West

Siberian precipitation during the last 50 years. *Atmos. Chem. Phys.*, 14(11):5853–5869.

Christner, E., Aemisegger, F., Pfahl, S., Werner, M., Cauquoin, A., Schneider, M., Hase, F., Barthlott, S., and Schädler, G. (2018). The climatological impacts of continental surface evaporation, rainout, and subcloud processes on δD of water vapor and precipitation in Europe. *J. Geophys. Res.: Atmos.*, 123(8):4390–4409.

Christner, E., Pfahl, S., Aemisegger, F., Werner, M., Cauquoin, A., Barthlott, S., Schneider, M., Steen-Larsen, H. C., Schädler, G., and Kottmeier, C. (2017). Modeling stable water isotopes in the Arctic region with $\text{COSMO}_{\text{iso}}$. Poster presented on 12th CLM-Community Assembly, Graz, A, September 19-22, 2017.

Craig, H. and Gordon, L. I. (1965). Deuterium and oxygen 18 variations in the ocean and the marine atmosphere. *Stable Isotopes in Oceanographic Studies and Paleotemperatures*, pages 9–130. E. Tongiorgi, Laboratorio di Geologia Nucleare, Pisa.

Dansgaard, W. (1964). Stable isotopes in precipitation. *Tellus*, 16(4):436–468.

Dütsch, M., Pfahl, S., Meyer, M., and Wernli, H. (2018). Lagrangian process attribution of isotopic variations in near-surface water vapour in a 30-year regional climate simulation over Europe. *Atmos. Chem. Phys.*, 18(3):1653–1669.

Dütsch, M., Pfahl, S., and Sodemann, H. (2017). The impact of nonequilibrium and equilibrium fractionation on two different deuterium excess definitions. *J. Geophys. Res.: Atmos.*, 122(23):12,732–12,746.

Dütsch, M., Pfahl, S., and Wernli, H. (2016). Drivers of δ^2H variations in an idealized extratropical cyclone. *Geophys. Res. Lett.*, 43(10):5401–5408.

Eckstein, J., Ruhnke, R., Pfahl, S., Christner, E., Diekmann, C., Dyroff, C., Reinert, D., Rieger, D., Schneider, M., Schröter, J., et al. (2018). From climatological to small-scale applications: Simulating water isotopologues with ICON-ART-Iso (version 2.3). *Geosci. Model Dev.*, 11:5113–5133.

Feng, X., Posmentier, E. S., Sonder, L. J., and Fan, N. (2018). Beyond Craig and Gordon: A model of water vapor isotopologues in the marine boundary layer. *Atmos. Chem. Phys. Discuss.* In review.

Galewsky, J., Steen-Larsen, H. C., Field, R. D., Worden, J., Risi, C., and Schneider, M. (2016). Stable isotopes in atmospheric water vapor and applications to the hydrologic cycle. *Rev. Geophys.*, 54(4):809–865.

Gat, J. R. (1996). Oxygen and hydrogen isotopes in the hydrologic cycle. *Annu. Rev. Earth Pl. Sc.*, 24(1):225–262.

Graf, P., Wernli, H., Pfahl, S., and Sodemann, H. (2019). A new interpretative framework for below-cloud effects on stable water isotopes in vapour and rain. *Atmos. Chem. Phys.*, 19(2):747–765.

Horita, J., Rozanski, K., and Cohen, S. (2008). Isotope effects in the evaporation of water: A status report of the Craig–Gordon model. *Isot. Environ. Healt. S.*, 44(1):23–49.

Joussaume, S., Sadourny, R., and Jouzel, J. (1984). A general circulation model of water isotope cycles in the atmosphere. *Nature*, 311(5981):24–29.

Jouzel, J. and Merlivat, L. (1984). Deuterium and oxygen 18 in precipitation: Modeling of the isotopic effects during snow formation. *J. Geophys. Res.*, 89(D7):11749–11757.

Merlivat, L. and Jouzel, J. (1979). Global climatic interpretation of the deuterium-oxygen 18 relationship for precipitation. *J. Geophys. Res.: Oceans*, 84(C8):5029–5033.

Morrison, A. K., Frölicher, T. L., and Sarmiento, J. L. (2015). Upwelling in the Southern Ocean. *Phys. Today*, 68(1):27–32.

Papritz, L., Pfahl, S., Sodemann, H., and Wernli, H. (2015). A climatology of cold air outbreaks and their impact on air–sea heat fluxes in the high-latitude South Pacific. *J. Climate*, 28(1):342–364.

Pfahl, S. and Wernli, H. (2008). Air parcel trajectory analysis of stable isotopes in water vapor in the eastern mediterranean. *J. Geophys. Res.: Atmos.*, 113(D20):D20104.

Pfahl, S. and Wernli, H. (2009). Lagrangian simulations of stable isotopes in water vapor: An evaluation of nonequilibrium fractionation in the Craig-Gordon model. *J. Geophys. Res.*, 114(D20):D20108.

Pfahl, S., Wernli, H., and Yoshimura, K. (2012). The isotopic composition of precipitation from a winter storm – a case study with the limited-area model $COSMO_{iso}$. *Atmos. Chem. Phys.*, 12(3):1629–1648.

Risi, C., Noone, D., Worden, J., Frankenberg, C., Stiller, G., Kiefer, M., Funke, B., Walker, K., Bernath, P., Schneider, M., et al. (2012). Process-evaluation of tropospheric humidity simulated by general circulation models using water vapor isotopologues: 1. Comparison between models and observations. *J. Geophys. Res.: Atmos.*, 117(D5):D05303.

Sharp, Z. (2007). *Principles of stable isotope geochemistry*. Pearson Prentice Hall.

Sodemann, H., Schwierz, C., and Wernli, H. (2008). Interannual variability of Greenland winter precipitation sources: Lagrangian moisture diagnostic and North Atlantic Oscillation influence. *J. Geophys. Res.*, 113(D3):D03107.

Sodemann, H. and Stohl, A. (2009). Asymmetries in the moisture origin of antarctic precipitation. *Geophys. Res. Lett.*, 36(22).

Sprenger, M. and Wernli, H. (2015). The LAGRANTO Lagrangian analysis tool – version 2.0. *Geosci. Model Dev.*, 8(8):2569–2586.

Steen-Larsen, H. C., Risi, C., Werner, M., Yoshimura, K., and Masson-Delmotte, V. (2017). Evaluating the skills of isotope-enabled general circulation models against in situ atmospheric water vapor isotope observations. *J. Geophys. Res.: Atmos.*, 122(1):246–263.

Steppeler, J., Doms, G., Schättler, U., Bitzer, H., Gassmann, A., Damrath, U., and Gregoric, G. (2003). Meso-gamma scale forecasts using the nonhydrostatic model LM. *Meteorol. Atmos. Phys.*, 82(1-4):75–96.

Stössel, A., Notz, D., Haumann, F. A., Haak, H., Jungclaus, J., and Mikolajewicz, U. (2015). Controlling high-latitude Southern Ocean convection in climate models. *Ocean Model.*, 86:58–75.

Sturm, C., Zhang, Q., and Noone, D. (2010). An introduction to stable water isotopes in climate models: Benefits of forward proxy modelling for paleoclimatology. *Clim. Past*, 6(1):115–129.

Taylor, K. E. (2001). Summarizing multiple aspects of model performance in a single diagram. *J. Geophys. Res.: Atmos.*, 106(D7):7183–7192.

von Storch, H., Langenberg, H., and Feser, F. (2000). A spectral nudging technique for dynamical downscaling purposes. *Mon. Weather Rev.*, 128(10):3664–3673.

Wei, Z., Lee, X., Aemisegger, F., Benetti, M., Berkelhammer, M., Casado, M., Caylor, K., Christner, E., Dyroff, C., García, O., et al. (2019). A global database of water vapor isotopes measured with high temporal resolution infrared laser spectroscopy. *Sci. data*, 6:180302.

Werner, M., Langebroek, P. M., Carlsen, T., Herold, M., and Lohmann, G. (2011). Stable water isotopes in the ECHAM5 general circulation model: Toward high-resolution isotope modeling on a global scale. *J. Geophys. Res.: Atmos.*, 116(D15):D15109.

Wernli, H. and Davies, H. C. (1997). A Lagrangian-based analysis of extratropical cyclones. I: The method and some applications. *Q. J. Roy. Meteor. Soc.*, 123(538):467–489.

Appendix

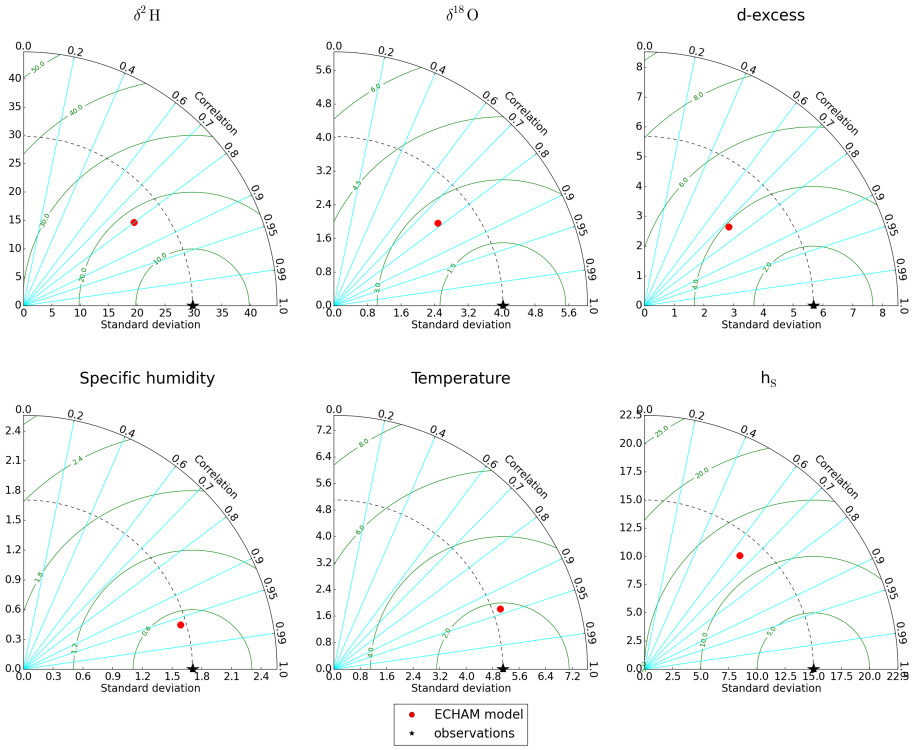

Fig. A1. Taylor diagrams of ECHAM5-wiso model data interpolated along Leg 2. Shown are diagrams for the isotopic variables δ^2H, δ^{18}O and d-excess as well as the meteorological variables specific humidity, temperature and h_S.

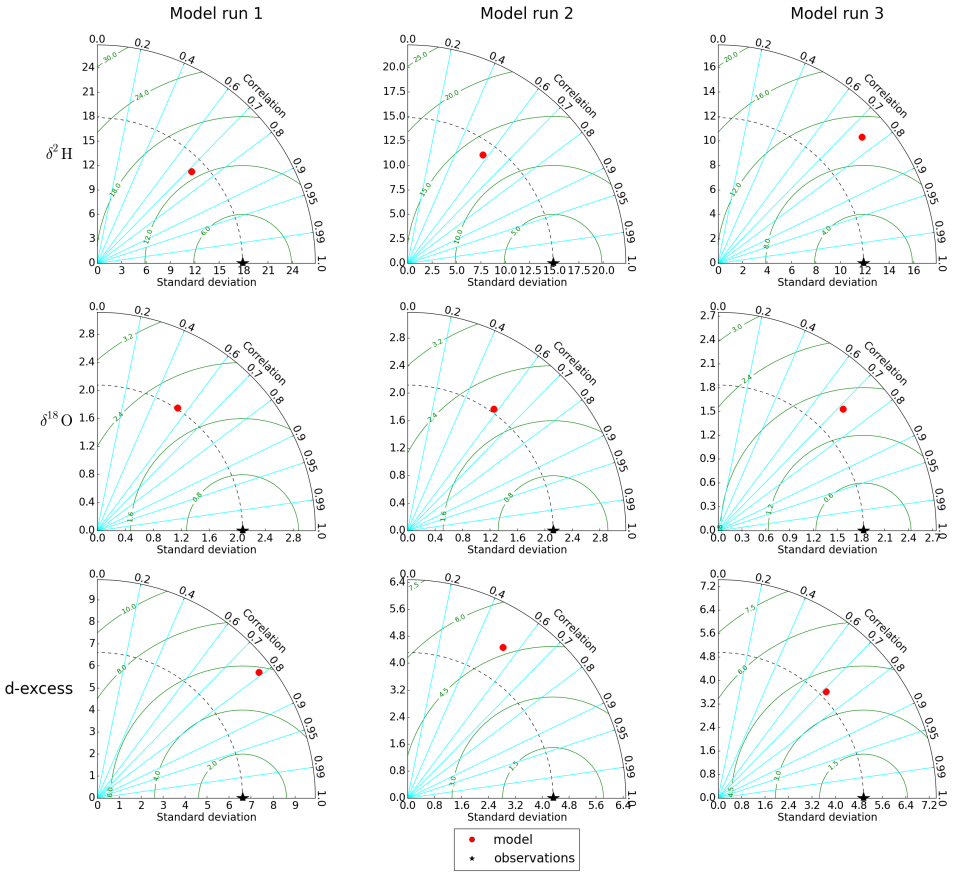

Fig. A2. Taylor diagrams of $COSMO_{iso}$ runs along Leg 1. Shown are diagrams for the isotopic variables δ^2H, $\delta^{18}O$ and d-excess.

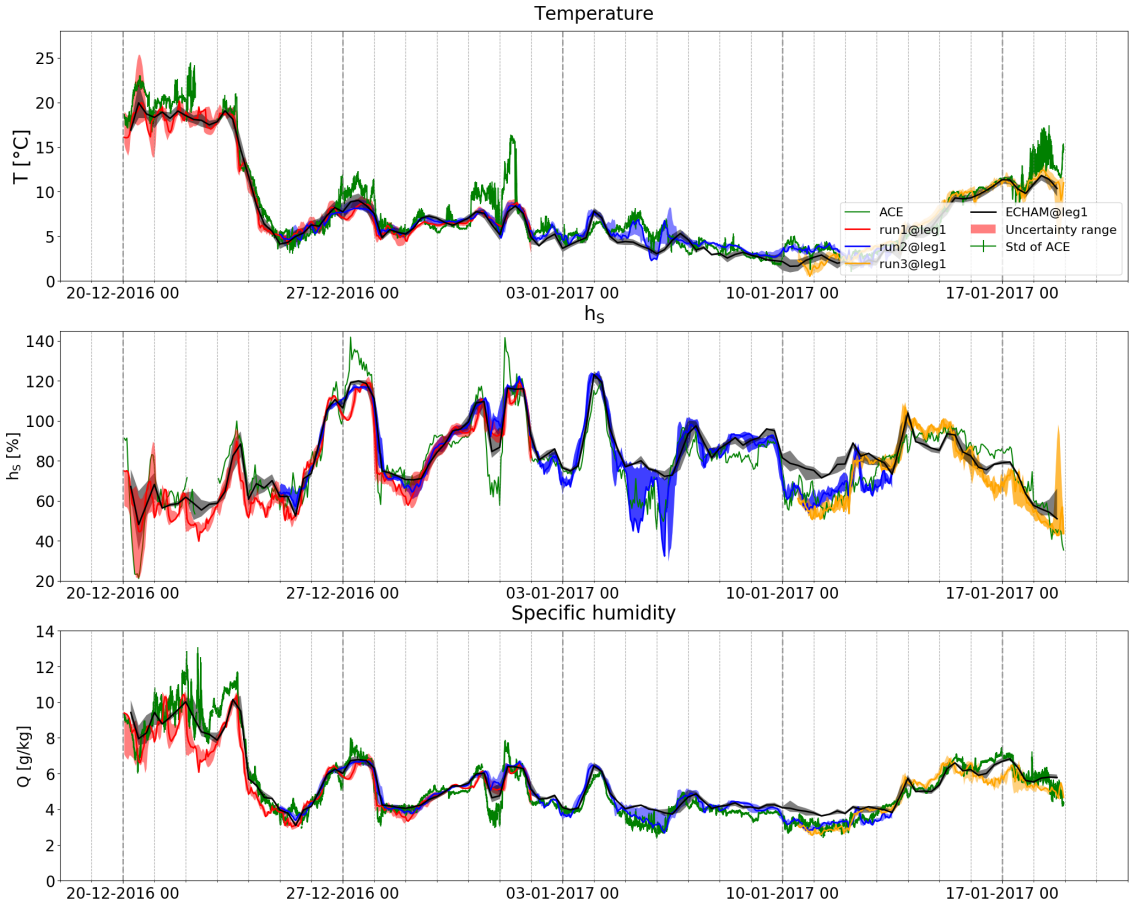

Fig. A3. Interpolation of meteorological variables temperature, h_S and specific humidity along Leg 1.

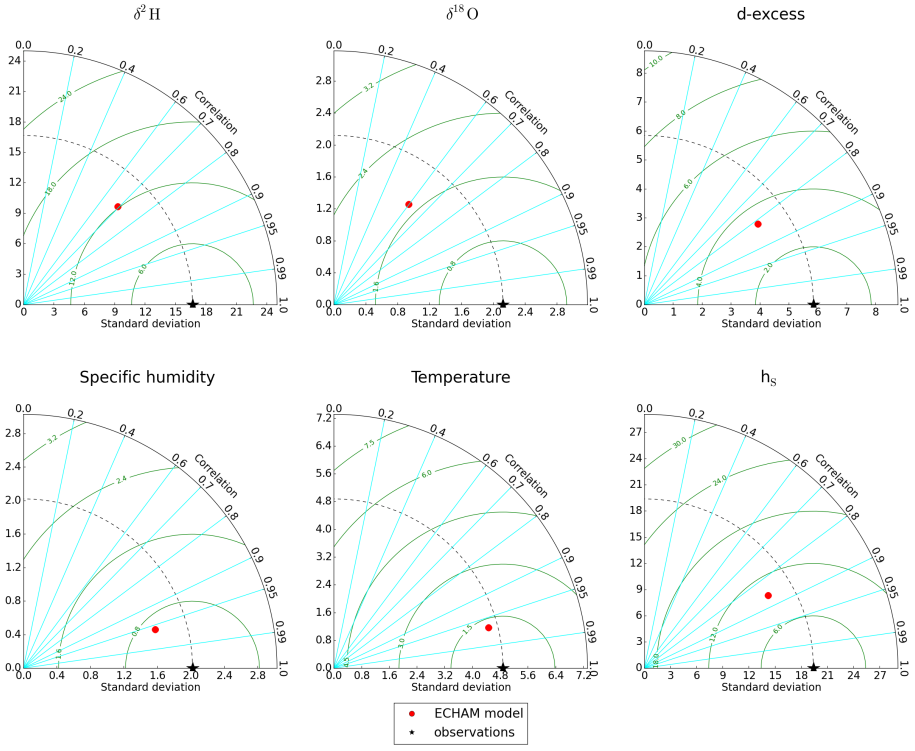

Fig. A4. Same as Figure A1 for Leg 1.

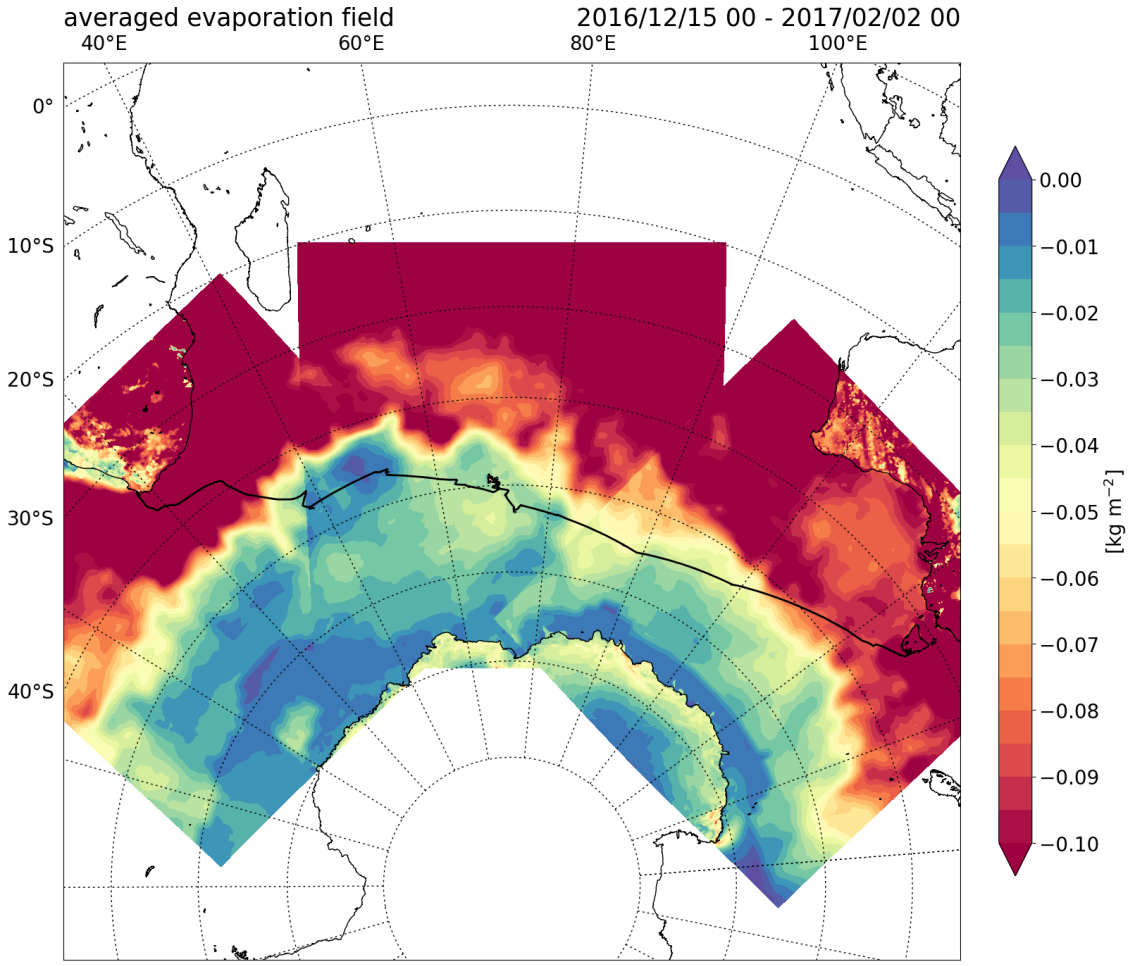

Fig. A5. Average ocean evaporation at each surface grid point. For each run the whole time period except for the first 2 days is considered.

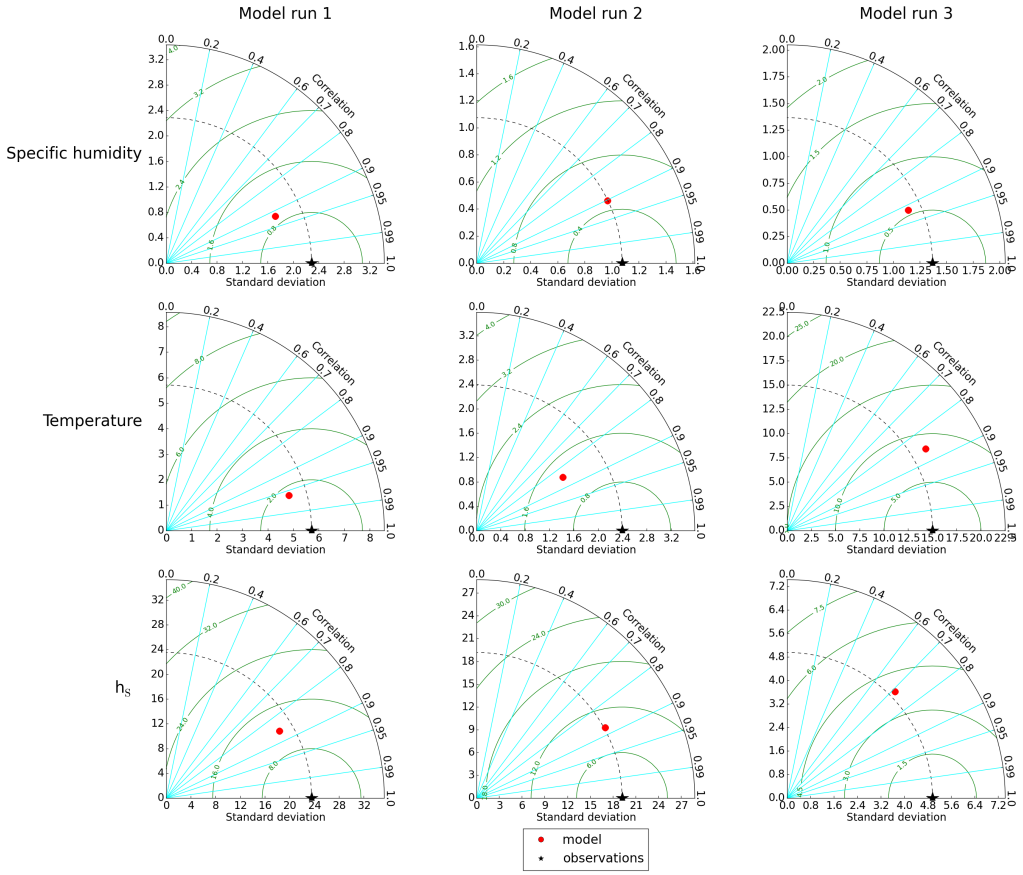

Fig. A6. Same as Figure A2 but for the meteorological variables specific humidity, temperature and h_S.

Acknowledgements

I want to express many thanks to Franziska Aemisegger, Iris Thurnherr and Fabienne Dahinden for offering me the possibility to dive into the topics of the atmospheric water cycle, stable water isotopes and isotope modelling. You guided me along the way but nevertheless gave me the freedom to pursue my own ideas. Your input, revisions and the joint discussions supported me a lot during the last months. Special thanks to...

...Franziska for our scientific discussions and your support in all matters, be it general input, feedback or technical assistance!

...Iris for your inputs regarding the measurements, your contribution to the simulations, your technical support and that you took your time for answering my questions on all sorts of topics.

...Fabienne for your technical guidance, which helped me a lot, for your revisions and valuable input.

Furthermore, I want to express my gratitude to the atmospheric dynamics group for giving me the opportunity to conduct my master thesis in a great working environment. A special appreciation is also owed to my fellow students from the office(s), which made the last months particularly enjoyable.

Finally, many thanks to my family for supporting me throughout my entire study time.

ETH

Eidgenössische Technische Hochschule Zürich
Swiss Federal Institute of Technology Zurich

Declaration of originality

The signed declaration of originality is a component of every semester paper, Bachelor's thesis, Master's thesis and any other degree paper undertaken during the course of studies, including the respective electronic versions.

Lecturers may also require a declaration of originality for other written papers compiled for their courses.

I hereby confirm that I am the sole author of the written work here enclosed and that I have compiled it in my own words. Parts excepted are corrections of form and content by the supervisor.

Title of work (in block letters):

Marine boundary layer stable water isotope variability in the Southern Ocean: An investigation using the regional COSMO$_{iso}$ model

Authored by (in block letters):

For papers written by groups the names of all authors are required.

Name(s):	**First name(s):**
Jansing	Lukas

With my signature I confirm that

- I have committed none of the forms of plagiarism described in the 'Citation etiquette' information sheet.
- I have documented all methods, data and processes truthfully.
- I have not manipulated any data.
- I have mentioned all persons who were significant facilitators of the work.

I am aware that the work may be screened electronically for plagiarism.

Place, date	**Signature(s)**
Zurich, March 26, 2019	L. Jansing

For papers written by groups the names of all authors are required. Their signatures collectively guarantee the entire content of the written paper.